bioRxiv preprint doi: https://doi.org/10.1101/2021.11.10.468007; this version posted February 27, 2022. The copyright holder for this preprint (which was not certified by peer review) is the author/funder. All rights reserved. No reuse allowed without permission.

A platform of patient-derived microtumors identifies therapeutic vulnerabilities in ovarian cancer.

Nicole Anderle[1]*, André Koch[2], Berthold Gierke[3], Anna-Lena Keller[1], Annette Staebler[4], Andreas Hartkopf[2], Sara Y. Brucker[2,5], Michael Pawlak[3], Katja Schenke-Layland[1,2,5,6,7], Christian Schmees[1]*

[1]NMI Natural and Medical Sciences Institute at the University of Tuebingen, Reutlingen, 72770 Germany.

[2]Department of Women's Health, Eberhard Karls University Tuebingen, Tuebingen, 72076 Germany.

[3]NMI Technologie Transfer GmbH, Pharmaservices Protein Profiling, Reutlingen, 72770 Germany.

[4]Institute of Pathology and Neuropathology, Eberhard Karls University Tuebingen, Tuebingen, 72076 Germany.

[5]Cluster of Excellence iFIT (EXC2180) "Image-Guided and Functionally Instructed Tumor Therapies", Eberhard Karls University Tuebingen, Tuebingen, 72076 Germany.

[6]Department of Biomedical Engineering, Eberhard Karls University Tuebingen, 72076 Tuebingen, Germany.

[7]Department of Medicine/Cardiology, Cardiovascular Research Laboratories, David Geffen School of Medicine at UCLA, Los Angeles, CA, 90095 USA.

* Nicole Anderle, Christian Schmees
Email: nicole.anderle@nmi.de, christian.schmees@nmi.de

bioRxiv preprint doi: https://doi.org/10.1101/2021.11.10.468007; this version posted February 27, 2022. The copyright holder for this preprint (which was not certified by peer review) is the author/funder. All rights reserved. No reuse allowed without permission.

Abstract

Background:

In light of the frequent development of therapeutic resistance in cancer treatment, there is a strong need for personalized model systems representing patient tumor heterogeneity, while enabling parallel drug testing and identification of appropriate treatment responses in individual patients. Using ovarian cancer as a prime example of a heterogeneous tumor disease with complex microenvironment and high recurrence rates, we developed a 3D preclinical ovarian cancer model comprised of patient-derived microtumors (PDM) and autologous tumor-infiltrating lymphocytes (TILs) for identification of treatment vulnerabilities and validation of anti-cancer drug efficacy using immunohistochemistry, immune cell phenotyping, functional assays and protein profiling analyses.

Methods:

PDM and TILs were isolated from fresh primary ovarian cancer tissue specimen using mechanical disruption and limited enzymatic digestion and were subsequently cultured in suspension in defined media in the absence of serum. The heterogeneous cellular composition of isolated PDM as well as autologous TILs was analyzed by FFPE immunohistochemistry and multi-color flow cytometry, respectively. For in-depth protein profiling of PDM we established Reverse Phase Protein Array (RPPA) analyses of >110 total and phospho-proteins. Treatment efficacy in response to chemotherapeutics as well as immunotherapeutic compounds was assessed in PDM and PDM-TIL co-cultures using a functional viability assay in microplate format.

Results:

The enzymatic digestion of primary ovarian cancer tissue and suspension culture in defined serum-free media allowed fast and efficient recovery of patient-derived microtumors (PDM). Immunohistochemical analyses demonstrated histopathological comparability of ovarian cancer PDM with corresponding patient tumor tissue. Reverse Phase Protein Array (RPPA)-based analyses of >110 total and phospho-proteins enabled the identification of patient-specific sensitivities to standard, platinum-based therapy and thereby the prediction of potential

bioRxiv preprint doi: https://doi.org/10.1101/2021.11.10.468007; this version posted February 27, 2022. The copyright holder for this preprint (which was not certified by peer review) is the author/funder. All rights reserved. No reuse allowed without permission.

treatment-responders. Finally, combining PDM and autologous TILs for individual efficacy testing of immune checkpoint inhibitor treatment demonstrated the potential for patient-specific enhancement of cytotoxic TIL activity by this therapeutic approach.

Conclusion:

3D patient-derived ovarian cancer microtumors represent a preclinical, ex vivo tumor model that reflects intertumoral heterogeneity and represent the cellular complexity of individual patient tumors. Combining protein pathway analysis and anti-cancer drug efficacy testing of PDM enables drug mode-of-action analyses and therapeutic sensitivity prediction within a clinically relevant time frame after surgery. Follow-up studies in larger cohorts are currently under way to further evaluate the applicability of this platform to support clinical decision-making and personalizing cancer treatment.

Keywords

Preclinical tumor model, ovarian cancer, anti-cancer drug efficacy testing, cancer immunotherapy, protein profiling, therapy resistance

Main Text

Background

In the context of personalized medicine, patient-derived model systems are expected to play an important role in order to identify suitable and effective therapies for the individual patient as well as existing therapeutic resistances of the patient's tumor. Especially for cancer types with dismal treatment success rates such as ovarian cancer (OvCa), these model systems will be valuable for future cancer therapy. OvCa is among the most lethal gynecological diseases in women with >185.000 deaths worldwide in 2018 (1). Late diagnosis and disease complexity characterized by strong molecular and genetic heterogeneity are causative for its poor survival rates and varying treatment response to first-line therapy. Substantial efforts have been made to resolve the complexity of OvCa, especially for high-grade serous carcinomas (HGSC) (2-4). Despite the application of genomics and transcriptomics in elucidating disease determinants, the principles of

bioRxiv preprint doi: https://doi.org/10.1101/2021.11.10.468007; this version posted February 27, 2022. The copyright holder for this preprint (which was not certified by peer review) is the author/funder. All rights reserved. No reuse allowed without permission.

responsiveness to therapy are still poorly understood (4). The establishment of patient-derived tumor organoids (PDO) allowed addressing a number of these challenges for example by in-depth genetic and phenotypic tumor characterization and analysis of intra-tumoral heterogeneity in PDOs side-by-side with corresponding tumor tissue (5-8). Even though recent studies have described the combination of PDO cultures with components of the tumor microenvironment including fibroblasts, endothelial cells and immune cells (9), PDOs do not fully reflect the original composition of primary tumor tissue in terms of extracellular matrix, tumor-associated fibroblasts, tumor-infiltrating lymphocytes (TILs), macrophages (TAMs), and tumor endothelial cells. Another challenge of current PDO models in terms of applicability for individualized drug response testing relates to the required establishment time of 1-3 months with a corresponding impact on the timeframe to obtain drug testing results (10). Using OvCa as a prime model of a heterogeneous tumor disease, we introduce a three-dimensional (3D) preclinical ex vivo model composed of patient-derived microtumors (PDM) as well as autologous tumor-infiltrating lymphocytes (TILs) extracted from primary OvCa tissue specimen in a clinical relevant time-frame. Importantly, PDM recapitulate a 3D histo-architecture with retained cell-cell contacts and native intra-tumoral heterogeneity featuring the corresponding primary tumor microenvironment (incl. extracellular matrix proteins, stromal fibroblasts and immune cells). In combination with functional compound efficacy testing and multiplexed TILs phenotyping, we demonstrate the correlation of individual OvCa PDM responses to chemotherapeutic as well as immunotherapeutic treatment approaches using OvCa PDM alone and in co-culture with autologous TILs, respectively. We apply Reverse Phase Protein Array (RPPA) analysis to map protein-signaling pathways of PDM and to measure on- and off-target drug effects in compound treated PDM. Albeit based on a small patient cohort the available clinical follow-up data suggests a correlation of obtained treatment responses in OvCa PDM models and corresponding patients indicating prolonged metastasis-free survival of identified carboplatin-responders as compared to non-responders.

bioRxiv preprint doi: https://doi.org/10.1101/2021.11.10.468007; this version posted February 27, 2022. The copyright holder for this preprint (which was not certified by peer review) is the author/funder. All rights reserved. No reuse allowed without permission.

Based on the data presented here, we envision that our preclinical assay system combining PDM, autologous TILs and protein signaling pathway profiling could aid clinical decision-making in the future and assist in the pre-selection of a personalized clinical treatment strategy for OvCa.

Materials and Methods

Human specimens

Ovarian tumor samples were obtained from nineteen patients diagnosed with ovarian cancer undergoing surgery at the Center for Women's Health, University Hospital Tuebingen. Written informed consent was obtained from all participants. The tumors were classified according to International Federation of Gynecology and Obstetrics (FIGO) grading system. Tumor samples were delivered on the day of operation. The research project was approved by the ethics committee (IRB#275/2017BO2 and IRB#788/2018BO2).

Isolation and cultivation of patient-derived microtumors and tumor-infiltrating lymphocytes

The procedure was adapted from Kondo et al. (2011) (11) and modified as follows. Tumor specimens were washed in HBSS (Gibco), minced with forceps, and digested with LiberaseTM DH (12) for 2h at 37°C. Digested tissue was centrifuged (300g, 5 min), washed with HBSS and filtered through a stainless 500 µm steel mesh (VWR). The flow-through was again filtered through a 40 µm cell strainer (Corning). The filtrate containing the TIL fraction was resuspended in Advanced RPMI 1640 (Gibco) supplemented with 2 mM Glutamine (Gibco), 1% MEM Vitamins (Gibco), 5% human serum (Sigma-Aldrich) and 100 µg/ml primocin (Invivogen). IL-2 (100 U/ml), IL-7 (10 U/ml) and IL-15 (23.8 U/ml) (Peprotech) were freshly added to culture media. For expansion, CD3/CD28 dynabeads were added (Milteny Biotech). PDM, held back by cell strainer, were washed in HBSS and cultured in suspension in StemPro® hESC SFM (Gibco) supplemented with 8 ng/ml FGF-basic (Gibco), 0.1 mM β-mercaptoethanol (Gibco), 1.8% BSA (Gibco) and 100 µg/ml primocin (Invivogen) within cell-repellent culture dish (60x15 mm) (Corning).

bioRxiv preprint doi: https://doi.org/10.1101/2021.11.10.468007; this version posted February 27, 2022. The copyright holder for this preprint (which was not certified by peer review) is the author/funder. All rights reserved. No reuse allowed without permission.

RPPA and protein data analysis

Detailed methods of sample preparation and RPPA processing are provided in SI Materials. RPPA protein analysis and protein data processing was applied as reported before (13-15). Detailed methods of sample preparation and RPPA processing are provided in SI Materials. From the arrays, PDM sample signals were extracted as protein-normalized, background-corrected mean fluorescence intensity (NFI), as measured from two technical sample replicates. NFI signals, median-centered for each protein over all measured samples (including OvCa PDM and BC PDM samples) and $\log_2$ transformed, reflect a measure for relative protein abundance. Small NFI protein signals at around blank assay level (0.02 NFI) were as a limiting quality criterion excluded from further analysis; otherwise all NFI signals were used for further protein data analysis. Protein heat maps were generated and cluster analysis (HCL) performed using the freely available MultiExperiment Viewer (MeV) software. For the comparison of protein profiles of treatment responders and non-responders (defined by functional compound testing), only proteins with a >20% difference between the means were used for analysis. On- and off-target pathway effects were evaluated from one biological and two technical replicate samples per model at three different treatment times (0.5, 4 and 72 h). Treated sample to respective DMSO vehicle control NFI ratios (TR) were calculated for each treatment condition and $\log_2$-transformed. A treatment-specific threshold of protein change (carboplatin: minimum 50% difference) was set. Only proteins showing treatment effects above the threshold were shown.

Efficacy of compounds validated in PDM cultures

Efficacy of compounds was validated by applying the real-time CellTox™ Green Cytotoxicity assay (Promega). Assays were performed according to manufacturer's protocol. PDM were cultured a maximum of 1-2 weeks in PDM culture medium prior testing. Per treatment three to eight replicates were performed using n = 15 PDM per replicate in a total volume of 150 µl phenol-red free PDM culture medium. Cell death was measured as relative fluorescent unit (RFU) (485–500 nm Ex / 520–530 nm Em), relative to the number of dead, permeable cells after 24h, 48h and 72h with the Envision Multilabel Plate Reader 2102 and Tecan Spark Multimode Plate

bioRxiv preprint doi: https://doi.org/10.1101/2021.11.10.468007; this version posted February 27, 2022. The copyright holder for this preprint (which was not certified by peer review) is the author/funder. All rights reserved. No reuse allowed without permission.

Reader. RFU values were normalized to DMSO control according to used drug solvent. Treatment effects were measured as fold change (FC) compared to control. Differences between treated PDM and untreated PDM were calculated as fold change values separately for each time point. Statistical significance was evaluated by two-way ANOVA multiple comparison test. Outliers were identified with the Iglewicz and Hoaglin's robust test for multiple outliers applying a recommended Z-score of ≥ 3.5 (16).

FACS analysis

To characterize lymphocyte populations within autologous TIL, cells were harvested (up to $1x10^6$ cells/staining depending on available number of cells), washed 2x with PBS (200 rpm, 5 min at 4°C), resuspended in staining buffer (PBS plus 10% FBS) and plated in a 96-well V-bottom plate (100 µl/well) (Corning). To verify >90% cell viability, cells were counted with a Nucleocounter (Chemotec) before plating. For each panel staining, an unstained control and if necessary a FMO control were prepared. For extracellular staining, cells were incubated with antibodies (see SI Materials) for 30 min at 4°C in the dark. For subsequent intracellular staining, cells were washed 2-3 times (200 rpm, 5 min at 4°C) in eBioscience™ Permeabilization buffer (250 µl/well) (Invitrogen) and resuspended in eBioscience™ Fixation/Permeabilization solution (Invitrogen) for 20 min at 4°C. After 2-3 washing steps (200 rpm, 5 min at 4°C), cells were incubated with antibodies (30 min, 4°C in dark) (see SI Materials). After the staining process, cells were washed 2-3 times and analyzed with a BD FACS Melody machine (BD Biosciences).

Co-culture of PDM and autologous TILs

To measure if the expanded, autologous TILs are able to kill corresponding PDM, we performed endpoint killing assays in a 96-well format with an image-based analysis using Imaris 8.0 software. First, PDM were pretreated with IFNγ (200 ng/ml) for 24 h to stimulate antigen presentation. In parallel, 96-well plates were coated with 5 g/ml of anti-CD28 antibody (Biolegend) o/n at 4°C to provide a co-stimulatory signal during co-culture. On the next day, coated plates were washed 3x with PBS. PDM were washed in HBSS, centrifuged and resuspended in co-

bioRxiv preprint doi: https://doi.org/10.1101/2021.11.10.468007; this version posted February 27, 2022. The copyright holder for this preprint (which was not certified by peer review) is the author/funder. All rights reserved. No reuse allowed without permission.

culture assay media consisting of RPMI 1640 phenol red free (GIBCO) supplemented with 2mM Glutamin (Gibco), 5% human serum (Sigma-Aldrich), 1x MEM Vitamins (Gibco) and 100 µg/ml Primocin (Invivogen). Prior of assembling the co-culture, TILs were labeled with CellTracker™ Deep Red Dye (Thermo Fisher Scientific) to differentiate between PDM and TILs. Labeled TILs were then co-cultured with PDM and in the presence of selected checkpoint immune inhibitors (CPIs: Pembrolizumab, Atezolizumab, Ipilimumab; Selleck Chemicals GmbH) or control anti-IgG4 antibody with an E:T ratio of 4:1. Thereby we counted 200 cells per single PDM. Per condition, we prepared triplicates each with 15 PDM and 12 000 TILs per well. After 92 hours, cells were incubated with a staining solution consisting of live cell stain Calcein-AM (Thermo Fisher Scientific) and Sytox™ Orange dead cell stain (Thermo Fisher Scientific). After 1 hour, Z-stacks of n = 3 PDM per well were imaged using a spinning disk microscope (ZEISS CellObserver Z1). Only viable PDM were positively stained by Calcein-AM, while all dead cells were stained by Sytox™ Orange. TILs were filtered by CellTracker™ Deep Red signal. Using the Imaris 8.0 software, we applied three masks, one for dead cells, one for dead TILs and one for live PDMs. For each mask, the total sum of all fluorescent intensities (FI) was calculated and the following ratio determined:

$$\%\, ratio\ dead\ vs. viable\ PDM\ [FI] = \frac{total\ dead\ [FI] - dead\ TIL\ [FI]}{viable\ PDM\ [FI]}$$

Statistical analysis

Statistical analysis was performed using GraphPad Prism. For Boxplot data, whiskers represent quartiles with minimum and maximum values and the median. Datasets with no clear normal distribution were analyzed with unpaired, two-tailed Mann-Whitney-U-test, otherwise as indicated. Correlation data were evaluated by Spearmans rank correlation. For all analyses, P values < 0.05 were considered statistically significant. Recommended post-hoc tests were applied for multiple comparisons.

bioRxiv preprint doi: https://doi.org/10.1101/2021.11.10.468007; this version posted February 27, 2022. The copyright holder for this preprint (which was not certified by peer review) is the author/funder. All rights reserved. No reuse allowed without permission.

Results

Isolation of patient-derived microtumors with high viability from primary OvCa tissue specimen by limited enzymatic digestion

Residual fresh tumor tissue samples were collected from n = 19 OvCa patients undergoing primary tumor debulking surgery. Available, anonymized clinico-pathological characteristics including International Federation of Gynecology and Obstetrics (FIGO) staging and pathological TNM-classification of respective individuals are summarized in Table 1.

Table 1. Clinical patient data from OvCa tumor specimen included into the study.

Sample OvCa #	Age at surgery	Histopathological classification	Cellular origin	Grade	FIGO stage	T	N	M	L	V	Pn	R	Isolated PDM
#1	53	HGSC	epithelial	HG	III	pT3c (liver/splenic capsule)	pN1a (2/14)	Mx	L1	V1	Pn1	Rx	yes
#3	88	HGSC	epithelial	HG	IIB	pT2b (peritoneum douglas)	Nx	Mx	L0	V0	Pn0	Rx	yes
#4	54	HGSC	epithelial	HG/G3	IIIC	ypT3c	ypN0	Mx	L0	V0	Pn0	Rx	yes
#5	59	HGSC	epithelial	HG/G3	IIIC	pT3c	pN1a (2/18)	Mx	L0	V0	Pn0	Rx	no
#7	67	HGSC	epithelial/peritoneal	HG	IVa	Tx	Nx	Mx	Lx	Vx	Pnx	Rx	yes
#8	44	MC	epithelial	LG	Ia	T1a	Nx	Mx	Lx	Vx	Pnx	Rx	yes
#11	84	HGSC	epithelial	HG/G3	IIIC	pT3c (peritoneal metastasis)	pN1a (2/6)	Mx	Lx	Vx	Pnx	R1	no
#12	81	FT	sex-chord/stromal	-	No indication for malignancy	Tx							no
#13	71	LGSC	epithelial	LG/G2	IIIC	pT3c	pN0	Mx	L0	V0	Pn0	Rx	yes
#16	60	HGSC	epithelial	HG/G3	IVb	ypT3b	ypN0	cM0	L1	V0	Pn0	R0	no
#17	62	HGSC	epithelial	HG	IIIC	pT3c	pN0	Mx	L1	V0	Pn0	Rx	yes
#18	61	HGSC	epithelial	HG/G3	IIIC	ypT3c	ypN0	cM0	L0	V0	Pnx	R0	yes
#19	60	HGSC	epithelial	HG/G3	IIIB	pT3b	pN0	cM0	L0	V0	Pn0	R0	yes
#20	66	HGSC	epithelial	HG	IVa	pT3c (pleural effusion)	pN1a	pM1a	L0	V0	Pn0	Rx	no
#21	74	adult-type GCT	sex-chord/stromal	-	IA	pT1a	pNx	cM0	L0	V0	Pn0	R0	yes
#23	71	HGSC	epithelial	HG/G3	IIIC	pT3c (Omentum metastasis)	pN1a	pMx	L1	V0	Pn0	Rx	yes
#24	73	HGSC	epithelial	HG	IIIC	pT3c	pN1b (58/75)	Mx	L1	V0	Pnx	R0	yes
#25	54	HGSC	epithelial	HG	IIA	pT2a (tube)	pN0	cM0	L0	V0	Pn0	cR0	yes
#26	67	HGSC	epithelial	HG/G3	IIIC	pT3c	pNx	Mx	L1	V0	Pn0	cR0	yes

FT, fibrothecoma; GCT, granulosa cell tumor; HGSC, high grade serous carcinoma; LGSC, low grade serous carcinoma; MC: mucinous carcinoma T: extent (size) of the tumor; N: spread to nearby lymph nodes; M: spread to distant sites; L, lymphatic invasion; V, venous invasion; Pn, perineural invasion; R, residual tumor; p, pathological state; c, clinical stage; y, restaged after neoadjuvant therapy; x, not assessed;

2/19 patients (OvCa #4 and OvCa #18) received neoadjuvant treatment with carboplatin/paclitaxel chemotherapy. The majority of included samples (n = 17) were derived from the most common type of OvCa, i.e. epithelial OvCa, with a majority of high-grade serous carcinomas (HGSC). Two samples were classified as sex-chord-stromal ovarian carcinomas that are either non-malignant or at a low stage. The PDM and TIL isolation procedure (further

bioRxiv preprint doi: https://doi.org/10.1101/2021.11.10.468007; this version posted February 27, 2022. The copyright holder for this preprint (which was not certified by peer review) is the author/funder. All rights reserved. No reuse allowed without permission.

developed from Kondo *et al.* 2011) (11) was performed on freshly excised tumor tissue specimen (Scheme 1).

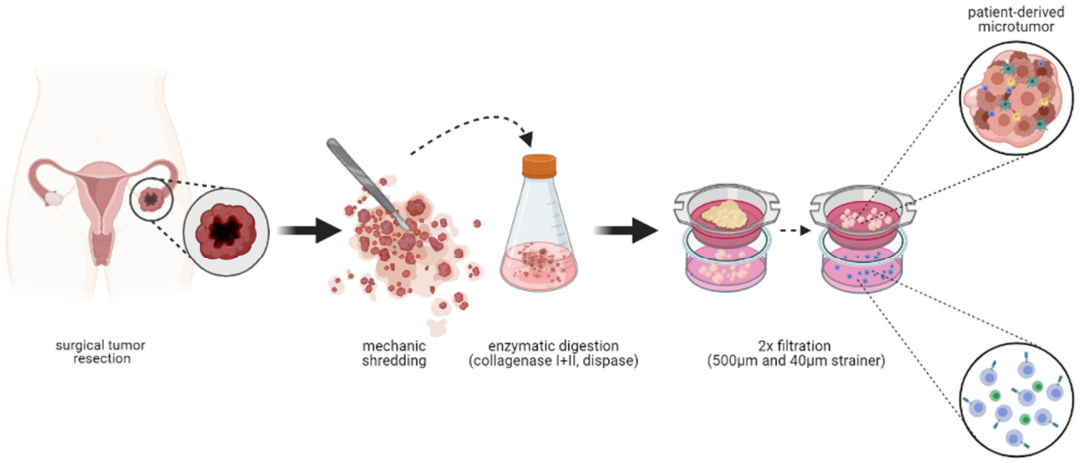

Scheme 1. PDM isolation from OvCa tumor samples within 3 hours after receipt of the tumor sample. Tumor tissue derived from surgical tumor resection is kept in culture media for transportation. Immediately after receipt of the sample, the tissue is mechanically disrupted into smaller pieces and enzymatically digested for 2 hours. Afterwards the digested tissue gets filtered twice using cell strainers. Within the first filtrate tumor-infiltrating lymphocytes are obtained ready for culturing or cryopreservation. From the residue of the second strainer, PDMs are gained ready for culturing or cryopreservation. (*Created with Biorender.com)*

Isolation of PDM a was successful in >70% (14/19) of the tumor samples (Fig. 1A) with varying amounts of available PDM for downstream analyses such as live-dead staining, immunohistochemical characterization, protein signaling pathway analyses and efficacy drug testing of standard-of-care therapy as well as immunotherapy (Scheme 2). PDMs were cultured in suspension in the absence of serum for a maximum of three weeks. No correlation was observed between successful isolation of PDM and available clinical patient data such as age, lymph node spread, distant cancer spread, perineural invasion or FIGO stage (Table S1). PDM viability was assessed by parallel staining with Calcein-AM and SYTOX™ Orange (Fig. 1B). 2D projections of 3D images displayed highly viable PDM with few dead cells. Dead PDM cells (according to nuclear SYTOX™ Orange staining) detached from PDM and thus observed mostly as single cells floating in the culture media. The quantification of the viable cell volume and dead cell volume in

bioRxiv preprint doi: https://doi.org/10.1101/2021.11.10.468007; this version posted February 27, 2022. The copyright holder for this preprint (which was not certified by peer review) is the author/funder. All rights reserved. No reuse allowed without permission.

3D projections of four exemplary OvCa PDM models are shown in Fig. 1C. In each analyzed model, ≤ 7% of the total PDM cell mass represented dead cells confirming robust PDM viability.

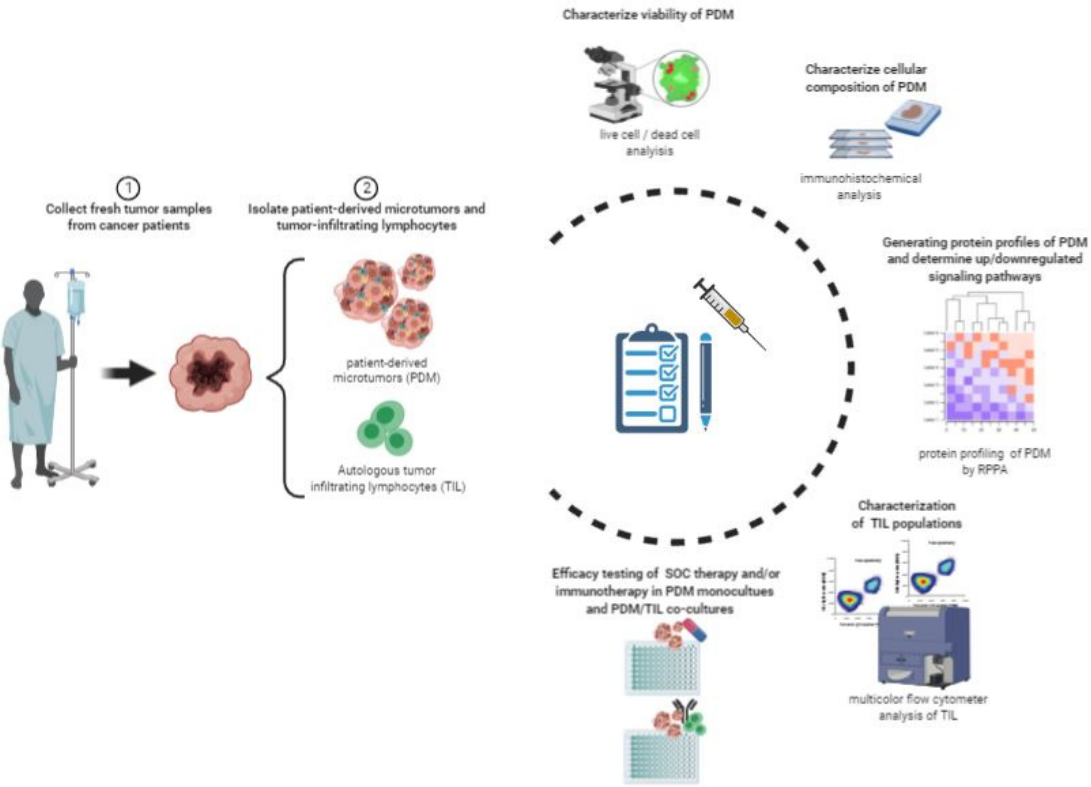

Scheme 2. Illustration of established downstream analyses of PDM and TILs. After the receipt of the tumor sample, PDM and TILs are immediately isolated and cultured. The viability of PDM is checked by a live/dead cell staining. Afterwards, the total number of available PDM is assessed. PDM are paraffin-embedded for immunohistochemical analyses. Anti-cancer drug efficacy is evaluated by measuring cytotoxicity in real-time requiring at least 300 PDM in total using 15 PDM per replicate (in total 4x). A minimum of 100-150 PDM are needed for further protein profiling analyses by RPPA. TILs are cultured and expanded for flow cytometry analyses as well as possible co-culture assays with PDM to assess immunotherapy sensitivity. Dependent on the total amount of PDM available, different downstream analyses are conducted and used for therapeutic sensitivity prediction. (*Created with Biorender.com)*

OvCa PDM sections resemble histopathological characteristics of the corresponding primary tumor tissue (PTT)

We next performed Hematoxylin and Eosin staining (H&E) of FFPE- and cryo-sections, respectively, derived from OvCa PDM and corresponding primary tumor tissue sections (PTT) for histopathological comparison. Professional assessment of PDM by a certified pathologist, confirmed typical, distinct histopathological characteristics of OvCa in respective PDM (Fig. 2 and Fig. S1). HGSC derived PDM reflected architectural patterns such as papillary growth, irregular branching, cystic and glandular structures (Fig. 2 OvCa #17-23; Fig. S1, OvCa #24, 26) as

bioRxiv preprint doi: https://doi.org/10.1101/2021.11.10.468007; this version posted February 27, 2022. The copyright holder for this preprint (which was not certified by peer review) is the author/funder. All rights reserved. No reuse allowed without permission.

compared to the corresponding PTT specimen. Pleomorphic nuclei/cells, high nucleus:cytoplasm ratio as wells as hyperchromasia were similar in PDM and corresponding PTT sections reflecting the high-grade of analyzed HGSC tumors. These tumor features were not detected within OvCa PDM #8 (Fig. S1), which originated from low-grade mucosal OvCa known for slow tumor growth. Instead, OvCa #8 PDM displayed a unicellular epithelium and mostly stromal remains. In summary, histopathological analyses of PDM confirmed structural and cellular similarities to the corresponding primary tumor specimen resembling typical histological features of ovarian carcinomas.

PDMs reflect intra- and intertumoral heterogeneity of the original tumor

For further characterization and study of the similarity of OvCa PDM and corresponding PTT, the expression of histotype specific markers, different tumor cell-, extracellular matrix- and immune cell-markers were assessed by immunohistochemistry (Fig. 2, Fig. S1). In the clinics, immunohistochemical staining of p53 and Wilms Tumor 1 (WT1) is applied for differential diagnosis of HGSCs (17). HGSC phenotype of the original tumor persists in the corresponding PDM as marker expression of WT1/p53 corresponded well with either low-to-moderate (OvCa #17-18) or strong expression (OvCa #23). Mesothelin (MSLN) and CA125 (MUC16) were used as additional OvCa markers. Mesothelin, known to be over-expressed on the cell surface in OvCa (18-20), was expressed in OvCa PDM mostly resembling expression of this marker in the corresponding PTT. Besides MSLN, CA125 expression has previously been described as an immunohistochemical marker to confirm ovarian origin of the tumor (21). As shown before (22, 23), expression of CA125 in OvCa sections can vary within one type and between the different OvCa tumor types. Accordingly, PTT sections derived from non-HGSC displayed no CA125 expression (OvCa #8) in contrast to HGSC-derived tumor sections (OvCa #17-18, #23-26). In PDM models OvCa#8, #17, #18 and #24 staining patterns of MSLN and CA125 were similar to corresponding PTT sections and were often restricted to cells at the tumor margin for CA125 (e.g. OvCa #18, #23). As the tumor microenvironment is known to play a major role in tumor progression and metastasis (24-26), we analyzed the presence of extracellular matrix (ECM) and

bioRxiv preprint doi: https://doi.org/10.1101/2021.11.10.468007; this version posted February 27, 2022. The copyright holder for this preprint (which was not certified by peer review) is the author/funder. All rights reserved. No reuse allowed without permission.

stromal components in OvCa PDM and corresponding PTT. Sections were stained for FAPα (Fibroblast associated protein alpha), a marker of activated fibroblasts, also known as cancer-associated fibroblasts (CAFs). FAPα expression in tumor stroma is observed in 90% of human cancers of epithelial origin and has been described to induce tumor progression and chemoresistance (27). FAPα staining in OvCa PDM mostly resembled that of the corresponding PTT in all samples except for OvCa #24-26 and differed from low to high expression. Collagen I expression, known to promote invasiveness and tumor progression in epithelial OvCa (28), was also prominent within OvCa PDM. Stainings correlated with corresponding PTT that showed an overall strong Collagen I expression except for OvCa #25. We also observed a strong correlation of Hyaluronan Binding Protein 1 (C1QBP) expression in PDM and corresponding PTT, which interacts with the major ECM component hyaluronan (29). In summary, all studied stromal components were found to be highly abundant within OvCA PDM and corresponding PTT. To further examine tumor microenvironmental (TME) components of PDM, we studied the infiltration with tumor-associated macrophages (TAMs) via CD163 expression together with the expression of the inhibitory checkpoint receptor ligand PD-L1. Analysis rarely detected M2-like TAMs ($CD163^+$) within PTT and PDM sections and if so, mostly in stromal tissue parts. While macrophages were highly frequent in OvCa #24 PTT, they were not detected in the corresponding PDM (Fig. S1). In contrast, for OvCa #17, $CD163^+$ TAMs were detected in both PDM and PTT sections (Fig. 2). Immune checkpoint receptor ligands are known to be expressed on tumor and/or immune cells of the tumor microenvironment. Here, PD-L1 expression was mostly absent in OvCa PTT and corresponding PDM sections. In conclusion, PDM largely resembled features of the original tumor by direct comparison with corresponding PTT including presence of complex ECM and TME architecture and expression of markers specific for OvCa. In comparison with corresponding PTT sections, pure stromal areas were mostly absent from stained PDM sections, which might explain differences observed between PDM and corresponding PTT with regard to immune cell infiltration and degree of expression of stromal components.

bioRxiv preprint doi: https://doi.org/10.1101/2021.11.10.468007; this version posted February 27, 2022. The copyright holder for this preprint (which was not certified by peer review) is the author/funder. All rights reserved. No reuse allowed without permission.

Protein signaling pathway profiling of OvCa PDM by RPPA

After initial immunohistochemical characterization of the 3D OvCa PDM that confirmed the presence of TME components in PDM similar to corresponding PTT, we performed an in-depth examination of the heterogeneity and molecular composition of different OvCa PDM models by generating signaling pathway protein profiles using RPPA. Protein abundances of 116 different proteins (including total and post-translationally modified forms) were measured in OvCa PDM samples each with a sample size of n = 100-150 per individual PDM (Fig. 3A). One further PDM sample derived from human BC (breast cancer) was included to scale up the protein sample data and for comparison as both cancer types are known to share molecular and microenvironmental similarities (26, 30). Obtained protein-normalized, background-corrected mean fluorescence intensity (NFI) signals were median-centered to all samples (n = 8) and $\log_2$ transformed. Protein profiles of PDM samples covered signaling pathways such as for cell cycle, DNA damage response, apoptosis, chromatin regulation, MAPK/RTK, PI3K/AKT with mTOR, Wnt and NFκB, as well as OvCa tumor/stem cell markers. By hierarchical clustering (HCL), PDM samples were grouped according to their similarities in relative protein signal intensity (Fig. 3A). Data analysis revealed three clusters: 1) OvCa #21 (OvCa granulosa cell tumor) and #23 (HGSC), with the most distinct protein profiles as compared to the other PDM analyzed; 2) OvCa #19 (HGSC) and the BC PDM shared more similarities than OvCa #19 with the other OvCa PDM models; 3). The remaining PDM samples resembled the third cluster with the most similar protein expression profiles containing exclusively HGSC models. Long distances of the sample dendrogram further underlines the proteomic heterogeneity of similar histopathological OvCa tumor types.

To compare protein abundances within different signaling pathways as well as of tumor/stem cell markers, proteins with impact on pathway activity were sorted according to their pathway affiliation (Fig. 3B, Table S2). Significant differences between PDM models were observed for the cell cycle pathway and the MAPK/RTK pathway. Highest cell cycle activity was found in OvCa #17 and #24 with almost 50% higher median NFI signals compared to OvCa #21 with the lowest median signals (median NFI = -0.33 $\log_2$) resembling a different histopathological tumor type

bioRxiv preprint doi: https://doi.org/10.1101/2021.11.10.468007; this version posted February 27, 2022. The copyright holder for this preprint (which was not certified by peer review) is the author/funder. All rights reserved. No reuse allowed without permission.

compared to the other PDM models analyzed. MAPK/RTK pathway signaling was increased in OvCa #21 (median NFI = 0.38 log_2), #23 (median NFI= 0.32 log_2), #24 (median NFI = 0.31 log_2) and #17 (median NFI = 0.30 log_2). The BC PDM model was characterized by decreased median NFI signals of MAPK/RTK proteins (median NFI = -0.47 log_2). Proteins related to PI3K/AKT pathway and of associated pathways were more abundant in OvCa #17 and #24. mTOR pathway levels were elevated in OvCa #24 (median NFI = 0.54 log_2) in other OvCa PDM this pathway showed comparable activity. Median NFI signals from apoptosis-related proteins were significantly different between OvCa #25 (median NFI = 0.75 log_2) and BC PDM (median NFI= 1.41 log_2). OvCa tumor/stem cell marker protein abundance was significantly upregulated in both OvCa #17 and #23 compared to BC PDM. Thus, RPPA protein profiling analysis demonstrated the heterogeneous activity of several signaling pathways within different OvCa PDM. Apoptosis-related proteins and OvCa tumor/stem cell marker proteins indicated the strongest differences between OvCa PDM models and the BC PDM model.

Heterogeneous treatment responses towards chemotherapy assessed by functional compound testing in OvCa PDM

Next, we used OvCa PDM as a platform for functional compound efficacy testing using standard-of-care chemotherapy treatment. Further, we sought to relate treatment responses in PDM to the generated protein profiling datasets. PDM were treated with carboplatin at up to three different concentrations (75, 100 and 125µM), chosen according to the previously reported C_{max} concentration of 135µM (31). Treatment efficacy in OvCa PDM – as measured by cytotoxicity - was heterogeneous among individual PDM models. Carboplatin induced the most significant cytotoxic effects at the lowest dose (75 µM) and longest treatment duration t = 72 h in OvCa #17 and #24 (Fig. 3C). On the molecular level, RPPA protein profiling revealed significantly increased cell cycle activity in both models (Fig. 3B), which might be associated with the comparably strong carboplatin response observed in OvCa PDM #17 and #24. OvCa #23 displayed reduced carboplatin sensitivity, with significant response observed after treatment at the highest dose of 125µM. Accordingly, OvCa #23 showed intermediate cell cycle activity in protein profiling

bioRxiv preprint doi: https://doi.org/10.1101/2021.11.10.468007; this version posted February 27, 2022. The copyright holder for this preprint (which was not certified by peer review) is the author/funder. All rights reserved. No reuse allowed without permission.

analyses (Fig. 3B). In conclusion, functional compound testing further confirmed the molecular heterogeneity of studied OvCa PDM models identified by protein profiling, which manifests in individual treatment responses to carboplatin.

Correlation of carboplatin treatment response and activation state of protein signaling pathways

To relate the analyzed protein signaling pathways of untreated OvCa PDM to observed treatment responses, protein NFI signals of PDM were grouped into responder and non-responder profiles according to significant treatment effects from functional compound testing (Fig. 3C). Mean protein signals (NFI) with >20% difference between responder and non-responder were plotted as heat map and significant differences of pathway signaling were analyzed. Further, we examined the on- and off-target pathway effects within different OvCa PDM models by RPPA to assess drug mode-of-action. For this aim, OvCa PDM were treated at one compound concentration and compared to vehicle (DMSO) control. Treatment-to-control signal ratios (TR) were determined from protein NFI signals of treated PDM samples and DMSO vehicle controls at three different time points for each treatment: immediate (30 min), early (4 h) and late (72 h). This enabled the exploration of fast and late treatment response based on changes of protein abundances within a given time frame.

Carboplatin treatment sensitivity of OvCa PDM correlates with high protein abundance of G2-M cell cycle proteins

HCL clustering of PDM protein NFI signals led to five clusters that distinguish carboplatin sensitive and resistant PDM models (Fig. 4A). To analyze significant differences related to activation or inactivation of signal transduction pathways, proteins from the HCL clustering were sorted according to their pathway affiliation and according to upregulation or downregulation in responder PDM models. Carboplatin-responder PDM models showed significantly increased cell cycle activity ($P < 0.001$; Fig. 4B) with upregulated protein abundance observed for Aurora A kinase (mean NFI = 0.74 $\log_2$), CDK2 (mean NFI = 0.8 $\log_2$), Cyclin B1 (mean NFI = 0.84 $\log_2$), PCNA (mean NFI = 0.84 $\log_2$), and acetylated Tubulin (mean NFI = 0.1 $\log_2$) (Fig. S2A), which

bioRxiv preprint doi: https://doi.org/10.1101/2021.11.10.468007; this version posted February 27, 2022. The copyright holder for this preprint (which was not certified by peer review) is the author/funder. All rights reserved. No reuse allowed without permission.

are mostly related to “mitosis” (32, 33). Aurora A (Spearman’s r = 0.912, *P* = 0.022), Cyclin B1 (Spearman’s r = 0.971, *P* = 0.011) and PCNA (Spearman’s r = 0.912, *P* = 0.022) significantly correlated with carboplatin treatment sensitivity (Table S3), which was graded according to recorded significance levels from “0-3” (“0”: *P* > 0.05; “1”: *P* < 0.05; “2”: *P* < 0.01; “3”: *P* < 0.001; Fig. 3C). At the same time, Carboplatin non-responder PDM models showed higher abundance of CDK1 (mean NFI = 0.38 $\log_2$), phospho-CDK2 (mean NFI = 0.77 $\log_2$) and phospho-CDK4 (mean NFI = 0.37 $\log_2$) (Fig. S2B), which are more related to the G0/G1 cell cycle phase. In addition, the apoptosis/DNA damage response pathway was significantly upregulated in Carboplatin-responder compared to non-responder PDM models (*P* = 0.021; Fig. 4B), especially with high abundance of cleaved Caspase-8 and cleaved PARP (Fig. S2A). Additional significant differences between Carboplatin responder and non-responder OvCa PDM were detected within the RTK and the PI3K/AKT/NFκB signaling pathways (*P* < 0.001; Fig. 4B). These pathways were downregulated in the Carboplatin non-responder group. Higher EMT/tumor/CSC marker abundance was significantly associated with the Carboplatin responder group (Fig. 4B) including protein markers Mesothelin, Nanog, STAT1, and E-Cadherin (Fig. S2A). In contrast, there were few proteins found, which were down-regulated in the carboplatin responder group. Collectively, this panel of down-regulated proteins differed significantly compared to the Carboplatin non-responder group (Fig. 4B). It contained early cell cycle markers e.g. Aurora A and Cyclin B1, the mTOR pathway effector phospho-S6RP, PDGFR and SNAI1. We further assessed metastasis-free-survival (MFS) between the described carboplatin responder (OvCa #17, #23-25) and non-responder (OvCa #19, #26) PDM models (Table S4). Metastasis-free-survival (MFS) analyses of available clinical follow-up patient data revealed prolonged median MFS of 16.2 month in Carboplatin responder vs. versus 9.2 months in Carboplatin non-responder models.

In summary, the activation state of different signaling pathways comprised of proteins with >20% difference in abundance, allowed to significantly distinguish carboplatin responder from non-responder OvCa PDM models. Importantly, these protein signaling response profiles were well in

bioRxiv preprint doi: https://doi.org/10.1101/2021.11.10.468007; this version posted February 27, 2022. The copyright holder for this preprint (which was not certified by peer review) is the author/funder. All rights reserved. No reuse allowed without permission.

line with results from functional compound efficacy testing assays using those OvCa PDM models.

Carboplatin treatment is associated with early induction of stress-response and late apoptosis

Next, we sought to investigate the carboplatin drug mode-of-action within OvCa PDM. Therefore, the carboplatin-responding OvCa PDM #24 was treated with carboplatin at a concentration of 75 µM, which had significantly induced PDM cytotoxicity in this model (see Fig. 3C). Protein NFI signals were measured at three different time points and normalized to vehicle control. Proteins revealing >50% difference in TR signals (Fig. S3) were selected to focus on the strongest changes in abundance. Cell cycle progression proteins (phospho-CDK2, CDK1) and phospho-Histone H3 (Ser10), affecting chromatin condensation during cell division, were downregulated quickly within 30 minutes (Fig. 4C). After 4 h of treatment, TR signals of phospho-Aurora A/B/C protein and Histone H3 was strongly increased (Fig. S3). Longer incubation with carboplatin (72 h) resulted in strong downregulation of these proteins (Fig. 4C). Diminished abundance of cell cycle proteins after 72 h of carboplatin treatment differed significantly from vehicle control ($P < 0.001$) and from early treatment (4 h; $P < 0.001$). While levels of cell cycle related proteins decreased over time, apoptotic markers such as cleaved-Caspases as well as acetylated p53 were elevated after 72 h (Fig. S3). Induction of apoptosis-related proteins was already observed after 4 h of treatment (Fig. 4C) with increasing abundances of cleaved Caspase 7 and acetylated p53 (Fig. S3). Focusing on down-stream PI3K/AKT/mTOR/Wnt pathway regulation, the abundances of mTOR effector proteins (S6RP, S6RP-phospho) were quickly upregulated after immediate (0.5 h) carboplatin treatment (Fig. S3), which is in line with previous reports about transcriptional regulation of stress response by the mTOR pathway (34). We also observed additional elevation of mTOR pathway-related proteins after 4 h of carboplatin treatment. Furthermore, overactive mTOR signaling might have resulted in increased p53 activation through upregulated acetylated p53 levels (Fig. S3) as described before (34). The PI3K/AKT/mTOR pathway was significantly upregulated within 4 h of carboplatin treatment compared to vehicle control ($P = 0.021$; Fig. 4C). Similar to proteins related to cell cycle, this pathway was completely

bioRxiv preprint doi: https://doi.org/10.1101/2021.11.10.468007; this version posted February 27, 2022. The copyright holder for this preprint (which was not certified by peer review) is the author/funder. All rights reserved. No reuse allowed without permission.

abrogated as compared to vehicle control after 72 h of treatment ($P < 0.001$; Fig. 4C). Changes in protein abundance differed significantly during all three measured time points (0.5 h vs. 4 h: $P = 0.003$; 4 h vs. 72 h and 0.5 h vs.72 h: $P < 0.001$ Fig. 4C). Pronounced, significant downregulation of MAPK/RTK pathway occurred after 72 h of treatment ($P = 0.017$; Fig. 4C). The observed proteomic changes within MAPK/RTK-related proteins over time were significant (0.5 h vs. 4 h: $P = 0.009$; 4 h vs. 72 h: $P < 0.001$; Fig. 4C). Thus, carboplatin treatment of OvCa #24 illustrated substantial and time-dependent changes in TR signals. Short treatment with carboplatin apparently triggered the induction of stress responses while longer treatment duration caused the induction of apoptosis.

Characterization of tumor-infiltrating lymphocyte populations from primary OvCa tissue samples

Our established procedure of tissue processing and PDM isolation enabled us to obtain single-cell suspensions containing tumor-infiltrating lymphocytes (TILs) from respective OvCa tumor specimen. This allowed for expansion of these autologous TILs in the presence of low-dosed cytokines and antigenic stimulation in order to investigate immuno-phenotypes of respective patient samples. The immunogenicity of OvCa has been demonstrated in prior studies and is confirmed by the frequent infiltration of ovarian tumors with TILs (35-37). As reported by Sato *et al*. (2005), different T cell populations diversely influence tumor immunosurveillance in OvCa. High intraepithelial $CD8^+/CD4^+$ T cell ratios in patients were associated with improved survival as $CD4^+$ T cells executed immunosuppressive functions. To determine the composition of the isolated immune cell infiltrate within our sample cohort, we characterized the phenotype of autologous TIL populations by multi-color flow cytometry (Fig. S4A). Within isolated and expanded OvCa TIL populations from different specimen, we found that the proportion of $CD4^+$ TILs was 57.8% and significantly more abundant than $CD8^+$ TILs with 33.5% ($P = 0.003$**; Fig. 5A, Table S5).

bioRxiv preprint doi: https://doi.org/10.1101/2021.11.10.468007; this version posted February 27, 2022. The copyright holder for this preprint (which was not certified by peer review) is the author/funder. All rights reserved. No reuse allowed without permission.

Isolated CD8$^+$ OvCa TILs are comprised of tumor-specific CD39$^+$, stem-like CD39$^-$PD1$^+$ and terminally differentiated CD39$^+$PD1$^+$ populations

Within the isolated CD8$^+$ TIL populations, we identified different phenotypes according to expression of the co-inhibitory receptors PD-1 and CTLA-4, the tumor-antigen specificity marker CD39 and the activation marker CD137 (Fig. 5A). To investigate the activation status of CD8$^+$ TILs, cells were examined for co-expression of the co-stimulatory receptor CD137 (4-1BB). CD137 is upregulated in activated T cells and has been suggested to be a marker for antigen-activated T cells (38). The mean percentage of CD8$^+$ CD137$^+$ TILs was 3.1% and varied between 0-10% (Table S5). >5% of the CD8$^+$ cytotoxic T-cells (CTLs) from OvCa #1, #3 and #5 (Fig. 5B) co-expressed CD137 indicating their pre-exposure to tumor antigens. Expression of co-inhibitory receptors PD-1 and CTLA-4 on CD8$^+$ TILs did not differ significantly among analyzed TIL populations but tended to higher PD-1 expression levels (mean 6.9% vs. 3.4%; Table S5). TILs from OvCa #3, #7 and #25 as well as #5, #13 and #26 were among those displaying an exhausted phenotype with >10% of CD8$^+$PD-1$^+$ or CD8$^+$CTLA-4$^+$ TILs (Fig. 5B). Moreover, in recent reports CD39 expression in CD8$^+$ TILs was described as a marker for tumor-antigen specific TILs that have undergone tumor-antigen-driven clonal expansion, exhibit resident memory T cell like phenotypes and express a variety of co-stimulatory and co-inhibitory receptors (39-41). Here, CD39$^+$ CTLs (mean 40.5%; range 4.4-96.8%, Table S5) were significantly more abundant than CD39$^-$ CTLs (mean 9.5%; range 0-48.3%, Table S5) so called 'bystander TILs' known to recognizing mostly viral antigens (40) ($P < 0.001$, Fig. 5A). The amount of CD39$^+$ TILs strongly correlated with the amount of CD8$^+$ TILs (Spearman $r = 0.88$, Fig. S4B; $P < 0.001$, Table S6) and conversely with the amount of CD4$^+$ TILs (Spearman $r = -0.80$, Fig. S4B; $P = 0.002$, Table S6). Thus, the abundance of CD4$^+$ and CD8$^+$ TILs appeared to significantly determine the amount of CD39$^+$ CTLs. In addition, CD39 expression was largely limited to CD8$^+$ TILs. As co-inhibitory receptors play a role in T cell exhaustion and are important targets for immune checkpoint-inhibition, we analyzed PD-1 and CTLA-4 expression on the tumor-specific CD39$^+$ CTL population. PD1$^+$CD39$^+$ were more frequent than CTLA-4$^+$ CD39$^+$ (15.7% vs. 5.4% Fig. 5A, Table S5). The total amount of CD8$^+$PD1$^+$ TILs thereby correlated with the amount of

bioRxiv preprint doi: https://doi.org/10.1101/2021.11.10.468007; this version posted February 27, 2022. The copyright holder for this preprint (which was not certified by peer review) is the author/funder. All rights reserved. No reuse allowed without permission.

$CD8^+CD39^+PD1^+$ TILs (Spearman *r* = 0.79, Fig. S4B; *P* = 0.002, Table S6) of a PDM model. Thus, CD39 expression was limited to tumor-antigen stimulated and exhausted TILs (e.g. OvCa #7, #17 and #25; Fig. 5B). In contrast to 'terminally differentiated cells' (42), OvCa TILs with a 'stem cell-like' $CD39^-PD1^+$ phenotype were found in 7.3% of the CTLs (Table S5). This population showed the highest proportional variability with a maximum of 50.5% cells vs. a minimum of 0% as compared to other $CD8^+$ TIL populations (CV 208%). The frequency of $CD8^+CD39^+$ and stem cell-like $CD8^+CD39^-PD1^+$ was negatively correlated (Spearman *r* = -0.63, Fig. S4B; *P* = 0.024, Table S6). These results confirm the feasibility of extracting and expanding TIL populations from fresh OvCa tissue samples and identify heterogeneous, patient-specific immuno-phenotypes with potential relevance for immuno-oncological treatment approaches.

Specific TIL phenotypes isolated from OvCa tumor specimen correlate with regional lymph node metastasis

We further analyzed the correlation between specific TIL populations and clinical follow-up patient data. OvCa patients with regional lymph node metastasis (N = 1) tended to present with significantly more extensive $CD8^+$ TIL infiltration in their tumors than those with no lymph node metastasis (N = 0) (*P* = 0.016) (Fig. 5C). Moreover, the frequency of $CD8^+$ TILs appeared to significantly correlate with that of $CD8^+CD39^+$ TILs in OvCa (Fig. 5C). Despite a small sample size, our data implicate a significant correlation between lymph node spread (N=1) and the presence of a $CD8^+CD39^+$ population (*P* = 0.008).

OvCa PDM killing by autologous TIL populations is enhanced by immune checkpoint inhibitor treatment

To evaluate the functional, tumor cell killing capacity of autologous TILs on OvCa PDM and the corresponding treatment efficacy of established immune checkpoint inhibitors (CPI), we subjected co-cultures of TILs and PDM from OvCa #24 and #26 to image-based analysis of CPI-treatment response. A total of nine PDM were imaged per treatment (3 PDM per well in triplicates) and a dead:live PDM ratio was calculated according to the sum of measured fluorescent intensities (FI) (Fig. 5D-F). Addition of TILs to autologous PDM induced a basal killing

bioRxiv preprint doi: https://doi.org/10.1101/2021.11.10.468007; this version posted February 27, 2022. The copyright holder for this preprint (which was not certified by peer review) is the author/funder. All rights reserved. No reuse allowed without permission.

effect in PDM in both models analyzed in the absence of CPI treatment (Fig. 5E-F). As the addition of matched isotype controls showed no additional effect in both co-culture models, we excluded the possibility of unspecific killing effects of CPI antibodies. TIL killing effects in OvCa #24 co-cultures were observed in response to treatment with either the combination of anti-PD1 and anti-CTLA-4 (pembrolizumab + ipilimumab) or anti-PD-L1 and anti-CTLA-4 (atezolizumab + ipilimumab) (P = 0.039) compared to isotype control treatment (Fig. 5E). Single agents induced no significant increase in PDM killing. In OvCa #26 CPI treatment almost doubled PDM killing (Fig. 5F). In comparison, co-cultures treated with ipilimumab (P = 0.004) or atezolizumab (P < 0.001) showed significant PDM killing compared to untreated PDM. The killing effect of TILs was significantly amplified by atezolizumab treatment compared to co-culture controls (PDM+TIL: P = 0.021; PDM+TIL+IgG4: P = 0.018; Fig. 5F), In line with this observation, respective OvCa PDM models showed weakly positive PD-L1 staining (Fig. S1). Further, atezolizumab treatment significantly increased the TIL killing effect towards PDM as compared to pembrolizumab (P = 0.026). Autologous CD8 TILs from both tested OvCa PDM models were composed of high amounts of tumor-specific, non-terminally differentiated $CD8^+CD39^+$ TIL populations as compared to other OvCa TILs (Fig. 5B). Moreover, these CD8 TILs were prominently positive for CTLA-4, which might explain the observed increase in PDM killing in response to ipilimumab (Anti-CTLA4) treatment (Fig. 5B) Thus, the co-culture of autologous TILs and PDM offers the possibility to extent compound efficacy testing beyond chemotherapeutic compounds to immune oncological treatment approaches in a patient-specific setting.

Discussion

Recently we could show the establishment of PDM from human glioblastoma tissue specimen containing important components of the tumor stroma (e.g. tumor-associated macrophages), and their application for the assessment of responses towards CSF1R- and PD1-targeting antibodies as well as the small molecule inhibitor Argyrin F (43, 44). In the present study, we have now further extended this approach to a patient-derived model system composed of PDM and autologous TILs extracted from a panel of primary OvCa tissue specimen and their in-depth

bioRxiv preprint doi: https://doi.org/10.1101/2021.11.10.468007; this version posted February 27, 2022. The copyright holder for this preprint (which was not certified by peer review) is the author/funder. All rights reserved. No reuse allowed without permission.

characterization by immunohistochemistry, protein profiling, immune cell phenotyping and focused compound efficacy testing. Our results show a 70% success rate for isolation of PDM with robust viability and in suitable amounts for further, multi-parametric downstream analyses. In-depth histopathological assessment of PDM sections confirmed the conservation of typical histological features of respective OvCa types by this model system. Importantly, the complexity of the ovarian cancer TME with respect to the presence of cancer-associated fibroblasts and extracellular matrix components incl. collagen and hyaluronan-binding protein observed in primary OvCa tissue sections was well conserved in PDM. The presence of these TME components has previously been correlated with tumor stage, prognosis, and progression and shown to substantially influence treatment responses (28, 45, 46). Interestingly, we could also identify immune cell infiltration within a subset of OvCa PDM, reflecting the immunogenicity of OvCa as previously reported (35, 36, 47).

While OvCa patient-derived organoids (PDO) were often studied by genomic and transcriptomic sequencing (6-8), we were the first (to our knowledge) to investigate inter-tumoral heterogeneity and differential drug response mechanisms by RPPA-based protein profiling in a patient-derived 3D OvCa preclinical cell model. Here, analyses of a panel of >110 phospho- and total proteins allowed for the clustering of histologically similar OvCa PDM models, pathway activity profiling and investigation of on- and off target drug effects. Obtained RPPA protein profiles confirmed the heterogeneity of OvCa PDM observed via immunohistochemistry and previously reported for HGSC, the most common type of OvCa. Our work identified significant differences in the activity of cell cycle and MAPK/RTK pathways within analyzed OvCa PDM and enabled their distinction from a breast cancer derived PDM model by differential expression of OvCa tumor and stem cell markers as well as apoptosis-related proteins.

Six OvCa PDM models were applied for individualized compound efficacy testing of standard of care platinum-based therapy. For analyzed OvCa PDM models, we observed patient-specific heterogeneity of response towards chemotherapy. Correlation with RPPA protein profiling data allowed the allocation of individual PDM drug responses to specifically up- or down-regulated

bioRxiv preprint doi: https://doi.org/10.1101/2021.11.10.468007; this version posted February 27, 2022. The copyright holder for this preprint (which was not certified by peer review) is the author/funder. All rights reserved. No reuse allowed without permission.

signaling pathway activities and enabled the prediction of PDM models with high probability of response towards chemotherapy. In accordance with the ability of cytostatic drugs to induce apoptosis especially in actively dividing cells (48), our work identified additional correlation between proteins relevant for S- and G2/M- cell cycle phase progression and carboplatin response. Specifically, our data implicate that elevated abundances of Aurora A, Cyclin B1 and PCNA proteins may allow for identification of carboplatin treatment response. Furthermore and in line with previous reports, we confirmed that decreased DNA damage repair and the ability to undergo apoptosis (49) is associated with carboplatin treatment sensitivity in OvCa. This was illustrated by increased levels of cleaved Caspase-7 and cleaved PARP. Our results did not identify a correlation of carboplatin-resistance and markers of cancer stem cells (CSCs) (50, 51) or epithelial-to-mesenchymal transition (EMT) (52, 53). Instead, we found the cancer stem cell-related protein Nanog as well N-Cadherin strongly upregulated in carboplatin responding PDM. These differing results might arise from the fact that above-mentioned previous studies were performed in adherent cell lines and not within a patient-derived 3D tumor model. Importantly, we identified protein signatures of OvCa PDM allowing for the identification and prediction of PDM models with high probability of response towards chemotherapy or targeted therapy. The correlation of our results with clinical data indicated a significant correlation of carboplatin treatment response with prolonged metastasis-free survival of respective patients. Given the small sample cohort analyzed here, these results need to be interpreted with caution but warrant further investigation.

We further assessed proteomic changes upon PDM treatment such as effects on protein abundance, directed on- and off-target pathway effects and drug mechanism-of-action within OvCa PDM. In a carboplatin sensitive PDM model, we observed a time-dependent decrease in cell cycle- and an increase in apoptosis-inducing protein abundance. In parallel, we found a fast stress response upon treatment as indicated by an activated mTOR pathway with high S6RP and active phospho-S6RP levels (34). Overactive mTOR in combination with cell stress and the

bioRxiv preprint doi: https://doi.org/10.1101/2021.11.10.468007; this version posted February 27, 2022. The copyright holder for this preprint (which was not certified by peer review) is the author/funder. All rights reserved. No reuse allowed without permission.

inability of cells to adapt to cellular stress might be responsible for p53 elevation (54, 55) and driving cells into senescence or apoptosis (56, 57).

Apart from testing the response of OvCa PDM to conventional chemotherapy, we sought to investigate the applicability of this model system for efficacy assessment of immuno-oncological treatment approaches. For this aim, we applied immunophenotyping of autologous TIL populations followed by their co-culture with respective PDM in the presence and absence of immunotherapeutic mono- and combination treatment schedules. Immunosurveillance of cancer strongly depends on the composition of tumor-infiltrated immune cells and the degree of tumor tissue infiltration and is known to influence treatment efficacies. As a result, the idea of an immunoscore, identifying a patient's immunophenotype, emerged (58). Our work uncovered several immunophenotypes within expanded TILs from OvCa patients by multicolor flow cytometry compared to previous immunohistochemistry based analysis (59). As described by Sato *et al*. (2005) (35) and Zhang *et al*. (2003) (36) high numbers of intraepithelial $CD8^+$ TILs are associated with better prognosis in OvCa. We found that OvCa TILs were largely composed of $CD4^+$ rather than $CD8^+$ TILs. In this regard, OvCa models with high amounts of suppressive $CD4^+$ TILs and low numbers of $CD8^+$ TILs are suggested to have worse prognosis (60). In line with previous reports (61), we identified expression of CD39 in OvCa TIL populations, a marker that distinguishes between tumor-specific CTLs ($CD39^+$) and bystander TILs ($CD39^-$) (39, 40). Interestingly, we found that $CD8^+$ TIL amounts correlated with that of $CD8^+$ $CD39^+$ TILs, and could confirm that these tumor-specific T cells constitute an exhausted, memory T cell like phenotype, as CD39 expression was limited to $CD8^+$PD-1^+ TILs. Importantly, our results further demonstrated that co-cultures of PDM and autologous TILs could be applied to assess treatment efficacy of CPIs in a patient-specific setting. Such PDM-TIL co-culture systems could potentially be used to identify OvCa patients more likely to respond to cancer immunotherapy. In the limited OvCa tumor tissue cohort investigated here, OvCa tumors with regional lymph node metastasis contained higher numbers of $CD8^+$ and $CD8^+CD39^+$ TILs. The co-culture models tested in our

bioRxiv preprint doi: https://doi.org/10.1101/2021.11.10.468007; this version posted February 27, 2022. The copyright holder for this preprint (which was not certified by peer review) is the author/funder. All rights reserved. No reuse allowed without permission.

study for response towards CPI treatment were derived from lymph-node spreading primary tumors, which might suggest that immunogenicity of OvCa increases upon metastasis. Limitations of our PDM model are currently the restricted number of PDM available from digestion of individual tumor tissue samples. From experience with different tumor types, an average of several hundred to several thousand microtumors can be isolated from fresh tissue samples. This number depends on the amount of tissue available for PDM isolation as well as tissue composition (including degree of fibrosis and necrosis). PDMs are therefore presently not suitable for high-throughput drug screening approaches, but for focused drug testing in late preclinical and translational drug development as well as in the context of precision oncology. Furthermore, the limitation of our present study with regard to sample size should be noted. In future follow-up studies with larger cohorts we plan to confirm our findings.

Conclusions

Patiend-derived microtumors isolated from OvCa tumor specimen represent a novel ex vivo tumor model for OvCa displaying histopathological similarities to corresponding primary patient tumors and revealing intertumoral heterogeneity as evidenced by immunohistochemical and protein profiling analyses. The combination of functional drug testing with analyses of protein signaling pathways and drug-mode of action enabled the identification of PDM models susceptible to platinum-based treatment and allowed for the prediction of individual therapeutic sensitivity. Parallel isolation and culturing of autologous TILs further allowed for the characterization of patient-individual immune-phenotypes as well as the assessment of responses towards immunotherapy in PDM-TIL co-cultures. While the rapid PDM/TIL extraction procedure and quick availability of resulting datasets within 3-4 weeks is in good accordance with timelines of clinical decision making, we plan to confirm our findings in future studies with larger sample cohorts.

bioRxiv preprint doi: https://doi.org/10.1101/2021.11.10.468007; this version posted February 27, 2022. The copyright holder for this preprint (which was not certified by peer review) is the author/funder. All rights reserved. No reuse allowed without permission.

List of abbreviations

PDM:	Patient-derived microtumors
TIL:	Tumor-infiltrating lymphocytes
FFPE:	Formalin-fixed paraffin-embedded
RPPA:	Reverse Phase Protein Array
OvCa:	Ovarian cancer
HGSC:	High-grade serous carcinoma
PDO:	Patient-derived organoids
TAM:	Tumor-associated macrophages
FIGO:	International Federation of Gynecology and Obstetrics
IL-2/7/15:	Interleukine-2/7/15
FGF-basic:	Basic fibroblast growth factor
BSA:	Bovine serum albumin
DMSO:	Dimethylsulfoxid
BC:	Breast cancer
HCL:	Hierarchical Clustering
MeV:	MultiExperiment Viewer
RFU:	Relative fluorescent unit
FC:	Fold change
PTT:	Primary tumor tissue
H&E:	Hematoxylin and Eosin staining
WT1:	Wilms tumor 1
MSLN:	Mesothelin
CA125:	Cancer-antigen 125
ECM:	Extracellular matrix
FAPα:	Fibroblast activation protein α
CAF:	Cancer associated fibroblast

bioRxiv preprint doi: https://doi.org/10.1101/2021.11.10.468007; this version posted February 27, 2022. The copyright holder for this preprint (which was not certified by peer review) is the author/funder. All rights reserved. No reuse allowed without permission.

C1QBP: Hyaluronan binding protein 1

TME: Tumor microenvironment

CPI: Checkpoint-inhibitors

CSC: Cancer-stem cells

bioRxiv preprint doi: https://doi.org/10.1101/2021.11.10.468007; this version posted February 27, 2022. The copyright holder for this preprint (which was not certified by peer review) is the author/funder. All rights reserved. No reuse allowed without permission.

Declarations

Ethics Approval and consent to participate

The study was conducted according to the guidelines of the Declaration of Helsinki and approved by the local Ethics Committee. The use of human samples was approved by the local Ethics Commission at the Medical Faculty of Tuebingen under the reference numbers IRB#275/2017BO2 and IRB#788/2018BO2. All patients enrolled gave their informed consent to participate in the study.

Consent for publication:

Not applicable.

Availability of data and material:

All data needed to evaluate the conclusions of the paper are included in this published article and its supplementary information file. Material and further data are available upon request after signature of an MTA from the corresponding authors.

Competing interests:

AH received consulting and speaking fees from GSK, AstraZeneca and Clovis. NA, AK, BG, ALK, AS, SYB, MP, KSL and CS declare no competing interests.

Funding:

This work received financial support from the Ministry of Baden-Wuerttemberg for Economic Affairs, Labor and Tourism (grant 3-4332.62-HSG/84).

Authors' contributions:

Conceptualization and design of the study: NA, CS, MP, KSL, SYB and AH; Data collection, data analysis, investigation and interpretation: NA, BG, MP, AK, ALK, AS, SYB and CS; Writing – original draft: NA and CS; Writing – review and editing: NA, CS, MP, ALK, KSL, AK, SYB, AH and AS; Visualization: NA, CS and SYB; Supervision: CS and AK; Project administration: NA, CS and AK; All authors have read and approved the final manuscript.

bioRxiv preprint doi: https://doi.org/10.1101/2021.11.10.468007; this version posted February 27, 2022. The copyright holder for this preprint (which was not certified by peer review) is the author/funder. All rights reserved. No reuse allowed without permission.

Acknowledgements:

We gratefully acknowledge the Department of Women's Health, Women's University Hospital, Tuebingen University Hospital for excellent support, helpful discussions and providing fresh tumor tissue biopsies and corresponding FFPE material. We thank all patients and healthy volunteers enrolled for giving their informed consent for secondary use of residual tissue, respectively.

References

1. Bray F, Ferlay J, Soerjomataram I, Siegel RL, Torre LA, Jemal A. Global cancer statistics 2018: GLOBOCAN estimates of incidence and mortality worldwide for 36 cancers in 185 countries. CA Cancer J Clin. 2018;68(6):394-424.
2. Izar B, Tirosh I, Stover EH, Wakiro I, Cuoco MS, Alter I, et al. A single-cell landscape of high-grade serous ovarian cancer. Nat Med. 2020;26(8):1271-9.
3. Network TCGAR. Integrated genomic analyses of ovarian carcinoma. Nature. 2011;474(7353):609-15.
4. Zhang H, Liu T, Zhang Z, Payne SH, Zhang B, McDermott JE, et al. Integrated Proteogenomic Characterization of Human High-Grade Serous Ovarian Cancer. Cell. 2016;166(3):755-65.
5. Verduin M, Hoeben A, De Ruysscher D, Vooijs M. Patient-Derived Cancer Organoids as Predictors of Treatment Response. Front Oncol. 2021;11(820):641980.
6. Chen H, Gotimer K, De Souza C, Tepper CG, Karnezis AN, Leiserowitz GS, et al. Short-term organoid culture for drug sensitivity testing of high-grade serous carcinoma. Gynecol Oncol. 2020;157(3):783-92.
7. Kopper O, De Witte CJ, Lõhmussaar K, Valle-Inclan JE, Hami N, Kester L, et al. An organoid platform for ovarian cancer captures intra- and interpatient heterogeneity. Nat Med. 2019;25(5):838-49.
8. Hill SJ, Decker B, Roberts EA, Horowitz NS, Muto MG, Worley MJ, Jr., et al. Prediction of DNA Repair Inhibitor Response in Short-Term Patient-Derived Ovarian Cancer Organoids. Cancer Discov. 2018;8(11):1404-21.
9. Neal JT, Li X, Zhu J, Giangarra V, Grzeskowiak CL, Ju J, et al. Organoid Modeling of the Tumor Immune Microenvironment. Cell. 2018;175(7):1972-88.e16.
10. Wensink GE, Elias SG, Mullenders J, Koopman M, Boj SF, Kranenburg OW, et al. Patient-derived organoids as a predictive biomarker for treatment response in cancer patients. npj Precision Oncology. 2021;5(1).
11. Kondo J, Endo H, Okuyama H, Ishikawa O, Iishi H, Tsujii M, et al. Retaining cell-cell contact enables preparation and culture of spheroids composed of pure primary cancer cells from colorectal cancer. Proc Natl Acad Sci U S A. 2011;108(15):6235-40.
12. Shuford S, Wilhelm C, Rayner M, Elrod A, Millard M, Mattingly C, et al. Prospective Validation of an Ex Vivo, Patient-Derived 3D Spheroid Model for Response Predictions in Newly Diagnosed Ovarian Cancer. Sci Rep. 2019;9(1):11153.
13. Pirnia F, Pawlak M, Thallinger GG, Gierke B, Templin MF, Kappeler A, et al. Novel functional profiling approach combining reverse phase protein microarrays and human

bioRxiv preprint doi: https://doi.org/10.1101/2021.11.10.468007; this version posted February 27, 2022. The copyright holder for this preprint (which was not certified by peer review) is the author/funder. All rights reserved. No reuse allowed without permission.

3-D ex vivo tissue cultures: expression of apoptosis-related proteins in human colon cancer. Proteomics. 2009;9(13):3535-48.

14. Pawlak M, Carragher NO. Reverse Phase Protein Arrays elucidate mechanisms-of-action and phenotypic response in 2D and 3D models. Drug Discovery Today: Technologies. 2017;23:7-16.

15. Kresbach GM, Pawlak M. High Precision RPPA: Concept, Features, and Application Performance of the Integrated Zeptosens Platform. Adv Exp Med Biol. 2019;1188:31-59.

16. Iglewicz B, Hoaglin DC. How to detect and handle outliers. Milwaukee, Wis.: Milwaukee, Wis. : ASQC Quality Press; 1993. ix, 87 p. p.

17. Köbel M, Rahimi K, Rambau PF, Naugler C, Le Page C, Meunier L, et al. An Immunohistochemical Algorithm for Ovarian Carcinoma Typing. Int J Gynecol Pathol. 2016;35(5):430-41.

18. Hilliard T. The Impact of Mesothelin in the Ovarian Cancer Tumor Microenvironment. Cancers (Basel). 2018;10(9):277.

19. Hassan R, Kreitman RJ, Pastan I, Willingham MC. Localization of Mesothelin in Epithelial Ovarian Cancer. Appl Immunohistochem Mol Morphol. 2005;13(3):243-7.

20. Chang M-C, Chen C-A, Chen P-J, Chiang Y-C, Chen Y-L, Mao T-L, et al. Mesothelin enhances invasion of ovarian cancer by inducing MMP-7 through MAPK/ERK and JNK pathways. Biochem J. 2012;442(2):293-302.

21. Tornos C, Soslow R, Chen S, Akram M, Hummer AJ, Abu-Rustum N, et al. Expression of WT1, CA 125, and GCDFP-15 as useful markers in the differential diagnosis of primary ovarian carcinomas versus metastatic breast cancer to the ovary. Am J Surg Pathol. 2005;29(11):1482-9.

22. Kriplani D, Patel MM. Immunohistochemistry: A diagnostic aid in differentiating primary epithelial ovarian tumors and tumors metastatic to the ovary. South Asian Journal of Cancer. 2013;02(04):254-8.

23. Neunteufel W, Breitenecker G. Tissue expression of CA 125 in benign and malignant lesions of ovary and fallopian tube: a comparison with CA 19-9 and CEA. Gynecol Oncol. 1989;32(3):297-302.

24. Cox TR. The matrix in cancer. Nature Reviews Cancer. 2021;21(4):217-38.

25. Bhat R, Bissell MJ. Of plasticity and specificity: dialectics of the microenvironment and macroenvironment and the organ phenotype. WIREs Developmental Biology. 2014;3(2):147-63.

26. Roskelley CD, Bissell MJ. The dominance of the microenvironment in breast and ovarian cancer. Semin Cancer Biol. 2002;12(2):97-104.

27. Mhawech-Fauceglia P, Yan L, Sharifian M, Ren X, Liu S, Kim G, et al. Stromal Expression of Fibroblast Activation Protein Alpha (FAP) Predicts Platinum Resistance and Shorter Recurrence in patients with Epithelial Ovarian Cancer. Cancer Microenviron. 2015;8(1):23-31.

28. Nissen NI, Karsdal M, Willumsen N. Collagens and Cancer associated fibroblasts in the reactive stroma and its relation to Cancer biology. J Exp Clin Cancer Res. 2019;38(1):115.

29. Saha P, Datta K. Multi-functional, multicompartmental hyaluronan-binding protein 1 (HABP1/p32/gC1qR): implication in cancer progression and metastasis. Oncotarget. 2018;9(12):10784-807.

bioRxiv preprint doi: https://doi.org/10.1101/2021.11.10.468007; this version posted February 27, 2022. The copyright holder for this preprint (which was not certified by peer review) is the author/funder. All rights reserved. No reuse allowed without permission.

30. Longacre M, Snyder N, Housman G, Leary M, Lapinska K, Heerboth S, et al. A Comparative Analysis of Genetic and Epigenetic Events of Breast and Ovarian Cancer Related to Tumorigenesis. Int J Mol Sci. 2016;17(5):759.
31. Liston DR, Davis M. Clinically Relevant Concentrations of Anticancer Drugs: A Guide for Nonclinical Studies. Clin Cancer Res. 2017;23(14):3489-98.
32. Ovejero S, Bueno A, Sacristán MP. Working on Genomic Stability: From the S-Phase to Mitosis. Genes. 2020;11(2):225.
33. Holder J, Poser E, Barr FA. Getting out of mitosis: spatial and temporal control of mitotic exit and cytokinesis byPP1 andPP2A. FEBS Lett. 2019;593(20):2908-24.
34. Aramburu J, Ortells MC, Tejedor S, Buxadé M, López-Rodríguez C. Transcriptional regulation of the stress response by mTOR. Science Signaling. 2014;7(332):re2.
35. Sato E, Olson SH, Ahn J, Bundy B, Nishikawa H, Qian F, et al. Intraepithelial CD8+ tumor-infiltrating lymphocytes and a high CD8+/regulatory T cell ratio are associated with favorable prognosis in ovarian cancer. Proc Natl Acad Sci U S A. 2005;102(51):18538-43.
36. Zhang L, Conejo-Garcia JR, Katsaros D, Gimotty PA, Massobrio M, Regnani G, et al. Intratumoral T Cells, Recurrence, and Survival in Epithelial Ovarian Cancer. New Engl J Med. 2003;348(3):203-13.
37. Hamanishi J, Mandai M, Iwasaki M, Okazaki T, Tanaka Y, Yamaguchi K, et al. Programmed cell death 1 ligand 1 and tumor-infiltrating CD8+ T lymphocytes are prognostic factors of human ovarian cancer. Proceedings of the National Academy of Sciences. 2007;104(9):3360-5.
38. Ye Q, Song DG, Poussin M, Yamamoto T, Best A, Li C, et al. CD137 Accurately Identifies and Enriches for Naturally Occurring Tumor-Reactive T Cells in Tumor. Clin Cancer Res. 2014;20(1):44-55.
39. Duhen T, Duhen R, Montler R, Moses J, Moudgil T, de Miranda NF, et al. Co-expression of CD39 and CD103 identifies tumor-reactive CD8 T cells in human solid tumors. Nat Commun. 2018;9(1):2724.
40. Simoni Y, Becht E, Fehlings M, Loh CY, Koo S-L, Teng KWW, et al. Bystander CD8+ T cells are abundant and phenotypically distinct in human tumour infiltrates. Nature. 2018;557(7706):575-9.
41. Canale FP, Ramello MC, Núñez N, Furlan CLA, Bossio SN, Serrán MG, et al. CD39 Expression Defines Cell Exhaustion in Tumor-Infiltrating CD8+T Cells. Cancer Res. 2018;78(1):115-28.
42. Jansen CS, Prokhnevska N, Master VA, Sanda MG, Carlisle JW, Bilen MA, et al. An intra-tumoral niche maintains and differentiates stem-like CD8 T cells. Nature. 2019;576(7787):465-70.
43. Przystal JM, Becker H, Canjuga D, Tsiami F, Anderle N, Keller A-L, et al. Targeting CSF1R Alone or in Combination with PD1 in Experimental Glioma. Cancers (Basel). 2021;13(10):2400.
44. Walter B, Canjuga D, Yüz SG, Ghosh M, Bozko P, Przystal JM, et al. Argyrin F Treatment-Induced Vulnerabilities Lead to a Novel Combination Therapy in Experimental Glioma. Advanced Therapeutics. 2021:2100078.
45. Yu G, Wang J. Significance of hyaluronan binding protein (HABP1/P32/gC1qR) expression in advanced serous ovarian cancer patients. 2013;94(1):210-5.
46. Yu H, Liu Q, Xin T, Xing L, Dong G, Jiang Q, et al. Elevated expression of hyaluronic acid binding protein 1 (HABP1)/P32/C1QBP is a novel indicator for lymph node and

bioRxiv preprint doi: https://doi.org/10.1101/2021.11.10.468007; this version posted February 27, 2022. The copyright holder for this preprint (which was not certified by peer review) is the author/funder. All rights reserved. No reuse allowed without permission.

peritoneal metastasis of epithelial ovarian cancer patients. Tumor Biol. 2013;34(6):3981-7.

47. Barnett B, Kryczek I, Cheng P, Zou W, Curiel TJ. Regulatory T cells in ovarian cancer: biology and therapeutic potential. Am J Reprod Immunol. 2005;54(6):369-77.

48. Valeriote F, van Putten L. Proliferation-dependent cytotoxicity of anticancer agents: a review. Cancer Res. 1975;35(10):2619-30.

49. Vasey PA. Resistance to chemotherapy in advanced ovarian cancer: mechanisms and current strategies. Br J Cancer. 2003;89(S3):23-8.

50. Haygood CLW. Ovarian cancer stem cells: Can targeted therapy lead to improved progression-free survival? World Journal of Stem Cells. 2014;6(4):441.

51. Bapat SA, Mali AM, Koppikar CB, Kurrey NK. Stem and Progenitor-Like Cells Contribute to the Aggressive Behavior of Human Epithelial Ovarian Cancer. Cancer Res. 2005;65(8):3025-9.

52. Deng J, Wang L, Chen H, Hao J, Ni J, Chang L, et al. Targeting epithelial-mesenchymal transition and cancer stem cells for chemoresistant ovarian cancer. Oncotarget. 2016;7(34):55771-88.

53. Liu S, Sun J, Cai B, Xi X, Yang L, Zhang Z, et al. NANOG regulates epithelial-mesenchymal transition and chemoresistance through activation of the STAT3 pathway in epithelial ovarian cancer. Tumor Biol. 2016;37(7):9671-80.

54. Lee CH, Inoki K, Karbowniczek M, Petroulakis E, Sonenberg N, Henske EP, et al. Constitutive mTOR activation in TSC mutants sensitizes cells to energy starvation and genomic damage via p53. The EMBO journal. 2007;26(23):4812-23.

55. Vadysirisack DD, Baenke F, Ory B, Lei K, Ellisen LW. Feedback control of p53 translation by REDD1 and mTORC1 limits the p53-dependent DNA damage response. Mol Cell Biol. 2011;31(21):4356-65.

56. Leontieva OV, Blagosklonny MV. DNA damaging agents and p53 do not cause senescence in quiescent cells, while consecutive re-activation of mTOR is associated with conversion to senescence. Aging (Albany NY). 2010;2(12):924-35.

57. Astle MV, Hannan KM, Ng PY, Lee RS, George AJ, Hsu AK, et al. AKT induces senescence in human cells via mTORC1 and p53 in the absence of DNA damage: implications for targeting mTOR during malignancy. Oncogene. 2012;31(15):1949-62.

58. Gajewski TF, Schreiber H, Fu Y-X. Innate and adaptive immune cells in the tumor microenvironment. Nat Immunol. 2013;14(10):1014-22.

59. Hwang WT, Adams SF, Tahirovic E, Hagemann IS, Coukos G. Prognostic significance of tumor-infiltrating T cells in ovarian cancer: a meta-analysis. Gynecol Oncol. 2012;124(2):192-8.

60. Curiel TJ, Coukos G, Zou L, Alvarez X, Cheng P, Mottram P, et al. Specific recruitment of regulatory T cells in ovarian carcinoma fosters immune privilege and predicts reduced survival. Nat Med. 2004;10(9):942-9.

61. Leem G, Park J, Jeon M, Kim E-S, Kim SW, Lee YJ, et al. 4-1BB co-stimulation further enhances anti-PD-1-mediated reinvigoration of exhausted CD39⁺ CD8 T cells from primary and metastatic sites of epithelial ovarian cancers. Journal for ImmunoTherapy of Cancer. 2020;8(2):e001650.

bioRxiv preprint doi: https://doi.org/10.1101/2021.11.10.468007; this version posted February 27, 2022. The copyright holder for this preprint (which was not certified by peer review) is the author/funder. All rights reserved. No reuse allowed without permission.

Figure legends

Figure 1. Patient-derived 3D microtumors (PDM) derived from primary OvCa tumor specimen show high viability (**A**) Efficiency of isolating OvCa PDM from a total of *n* = 19 fresh primary OvCa tumor tissues samples. PDM were isolated from *n* = 14 specimen with a success rate of 73.7%. (**B**) Viability of OvCa PDM models. Exemplary 2D images from 3D projections of *n* = 4 OvCa PDM models confirm high viability according to Calcein-AM (viable cells) and SYTOX™ Orange (dead cells) staining. (**C**) Percentage of viable and dead cells in OvCa PDM. Viability was assessed by an image-based analysis (see SI Methods) in *n* = 4 OvCa PDM models shown in (B). Data are shown as mean values with SEM from at least *n* = 3 PDM of each model. **P* < 0.05, ***P* < 0.01, ****P* < 0.001, multiple paired t-test with Holm-Šídák's post hoc test. Scale bar 50 µm.

Figure 1. OvCa PDM resemble histopathological features of the corresponding primary tumor tissue. Hematoxylin and Eosin (H&E) staining of OvCa PDM and corresponding primary tumor tissue (PTT) sections revealed features of malignant cells (incl. giant cells with more than one nucleolus, hyperchromatic cells with dark nuclei and high nuclei:cytoplasma ratio) confirming the cancerous origin. Qualitative characterization of OvCa PDM was performed by DAB immunohistochemical staining of FFPE sections (3 µm). Expression of OvCa histotype specific markers (p53, WT1), tumor markers (CA125, MSLN), tumor-associated macrophages (CD163), immune/tumor marker (PD-L1), cancer-associated fibroblasts (FAPα) and extracellular matrix components (Hyaloronan C1QBP, Collagen I) within PDMs is shown. Scale bars indicate 500 µm for PTT; 50 µm for PDM; 20 µm for magnifications (PTT and PDM). FAPα, cancer-associated fibroblast protein alpha; C1QBP, hyaluronan binding protein; WT1, wilms tumor 1; MSNL, mesothelin.

Figure 3. RPPA protein profiling of OvCa PDM identifies significant differences in active protein signaling pathways as molecular basis for OvCa PDM drug treatment responses. (**A**) Protein heat map covering 116 analytes analyzed in OvCa PDM (*n* = 7) and BC PDM (*n* = 1) generated from sample sizes of *n* = 100-150 PDM. Protein abundances for each analyte are

bioRxiv preprint doi: https://doi.org/10.1101/2021.11.10.468007; this version posted February 27, 2022. The copyright holder for this preprint (which was not certified by peer review) is the author/funder. All rights reserved. No reuse allowed without permission.

displayed as median-centered, log_2-transformed NFI signals. Samples were subjected to hierarchical clustering using Euclidean distance (complete linkage). (**B**) Activation state of different pathways in the different OvCa PDM models. Proteins related to an "active" pathway were selected for each of the plotted pathways (see Table S4). Protein signals are shown as median-centered, log_2 transformed NFI signals. Dotted lines indicate log_2 values of +0.6 (fold change of +1.5) and -1 log_2 (fold change of -0.5). Data are shown as box and whiskers plots with minimum and maximum range. *$P < 0.05$, **$P < 0.01$, ***$P < 0.001$, Kruskal-Wallis test with Dunn's post hoc test. (**C**) Cytotoxicity measurement of indicated OvCa PDM models treated with standard platinum-based chemotherapy (Carboplatin; final concentrations 75, 100 and125 µM). Four replicates per treatment with n = 15 PDM per well were performed and measured after 24 h, 48 h and 72 h. Signals were measured as RFU (Relative Fluorescent Unit), background corrected and normalized to vehicle control (DMSO). Data are shown as mean values. Statistical significances compared to vehicle control or H_2O are shown. *$P < 0.05$, **$P < 0.01$, ***$P < 0.001$, Two-way ANOVA with Bonferroni's multiple comparison test. Carbo: carboplatin

Figure 4. Carboplatin drug response in OvCa PDM correlates with the activity of diverse signaling pathways. (**A**) Heat map of protein abundances (calculated from median-centered NFI values) averaged over carboplatin responder and non-responder OvCa PDM. Carboplatin responders and non-responders were grouped according to significant treatment effects from functional compound testing (Fig. 3C). Only proteins with >20% increased or decreased abundance between responder and non-responder group were selected. Data was HCL clustered with Euclidean distance (average linkage). (**B**) Signaling pathway activation in carboplatin responder vs. non-responder OvCa PDM. Proteins were sorted according to their pathway affiliation and according to upregulation or downregulation within responder group. *$P < 0.05$, **$P < 0.01$, ***$P < 0.001$, Mann-Whitney-U-test. R, responder; Non-R, Non-responder. (**C**) Proteomic on- and off-target pathway effects in carboplatin-treated (75 µM) OvCa #24 PDM analyzed by RPPA. Treated PDM were analyzed from an immediate (0.5 h), an early (4 h) and a late (72 h) treatment time. For each time point, protein values are displayed as log_2-transformed treatment-

bioRxiv preprint doi: https://doi.org/10.1101/2021.11.10.468007; this version posted February 27, 2022. The copyright holder for this preprint (which was not certified by peer review) is the author/funder. All rights reserved. No reuse allowed without permission.

to-control signal ratios (TR) calculated from NFI signals of treated PDM and corresponding vehicle control (DMSO). Only proteins with >50% differential protein abundance compared to vehicle control were selected. Straight lines above plots indicate statistical significances compared to vehicle control. *P < 0.05, **P < 0.01, ***P < 0.001, One-way ANOVA using nonparametric Kruskal-Wallis with Dunn's ad hoc test.

Figure 5. CPI treatment in OvCa PDM-TIL co-cultures increased functional TIL killing capacity. Autologous TIL populations were isolated and expanded from OvCa tissue specimen. (**A**) Percentages of different TIL populations within CD3, CD8 and CD4 positive T cells of different models were quantified by multicolor flow cytometry. Data are shown as means ± SEM of at least n = 10 OvCa samples. *P < 0.05, **P < 0.01, ***P < 0.001, ANOVA with Holm-Šídák's post hoc test. (**B**) Phenotypes of extracted TIL populations shown separately for each OvCa model. Pembro: pembrolizumab 60 µg/ml; Ipilim: ipilimumab 50 µg/ml; Atezo: atezolizumab 50 µg/ml. (**C**) Percentages of $CD8^+$ and $CD8^+CD39^+$ TILs in OvCa patients with lymph node spread (N = 1) and without lymph node spread (N = 0). All points with median are shown. *P < 0.05, **P < 0.01, Mann-Whitney-U-test. (**D**) PDM killing effects were measured in an image-based assay format as ratio of fluorescent intensities (FI) of dead cells vs. live PDM cells. Per treatment n = 3 PDM in three replicates were analyzed. Masks for viable PDM (Calcein-AM staining), dead cells (SYTOX™ Orange dead cell staining) and TILs (CellTracker™ Deep Red staining) were applied using Imaris 8.0 software. Scale bars indicate 50 µm. FI from TILs were subtracted from the total dead FI. (**E-F**) Killing effects of autologous TILs on corresponding PDM in co-cultures treated with immune checkpoint inhibitors (CPI). TILs of OvCa #24 (**D**) and #26 (**E**) were co-cultured with n = 15 PDM using an E:T ratio of 4:1 and treated with CPI either alone or in combination. *P < 0.05, **P < 0.01, ***P < 0.001, ANOVA with Holm-Šídák's post hoc test.

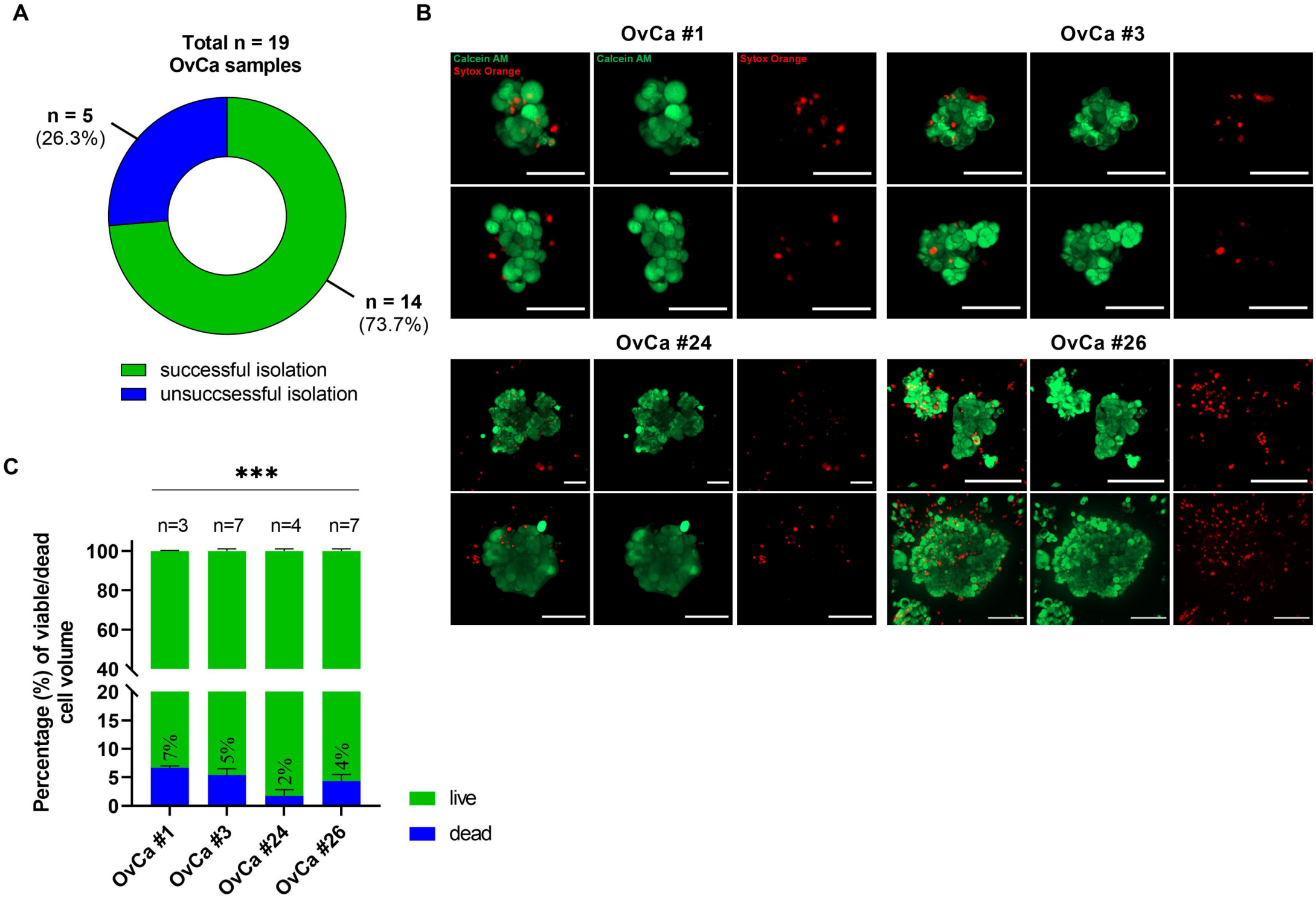
A
Total n = 19
OvCa samples
n = 5
(26.3%)
n = 14
(73.7%)
successful isolation
unsuccsessful isolation
B
OvCa #1
OvCa #3
OvCa #24
OvCa #26
Calcein AM
Sytox Orange
C
***
n=3
n=7
n=4
n=7
Percentage (%) of viable/dead cell volume
100
80
60
40
20
15
10
5
0
7%
5%
2%
4%
OvCa #1
OvCa #3
OvCa #24
OvCa #26
live
dead

bioRxiv preprint doi: https://doi.org/10.1101/2021.11.10.468007; this version posted February 27, 2022. The copyright holder for this preprint (which was not certified by peer review) is the author/funder. All rights reserved. No reuse allowed without permission.

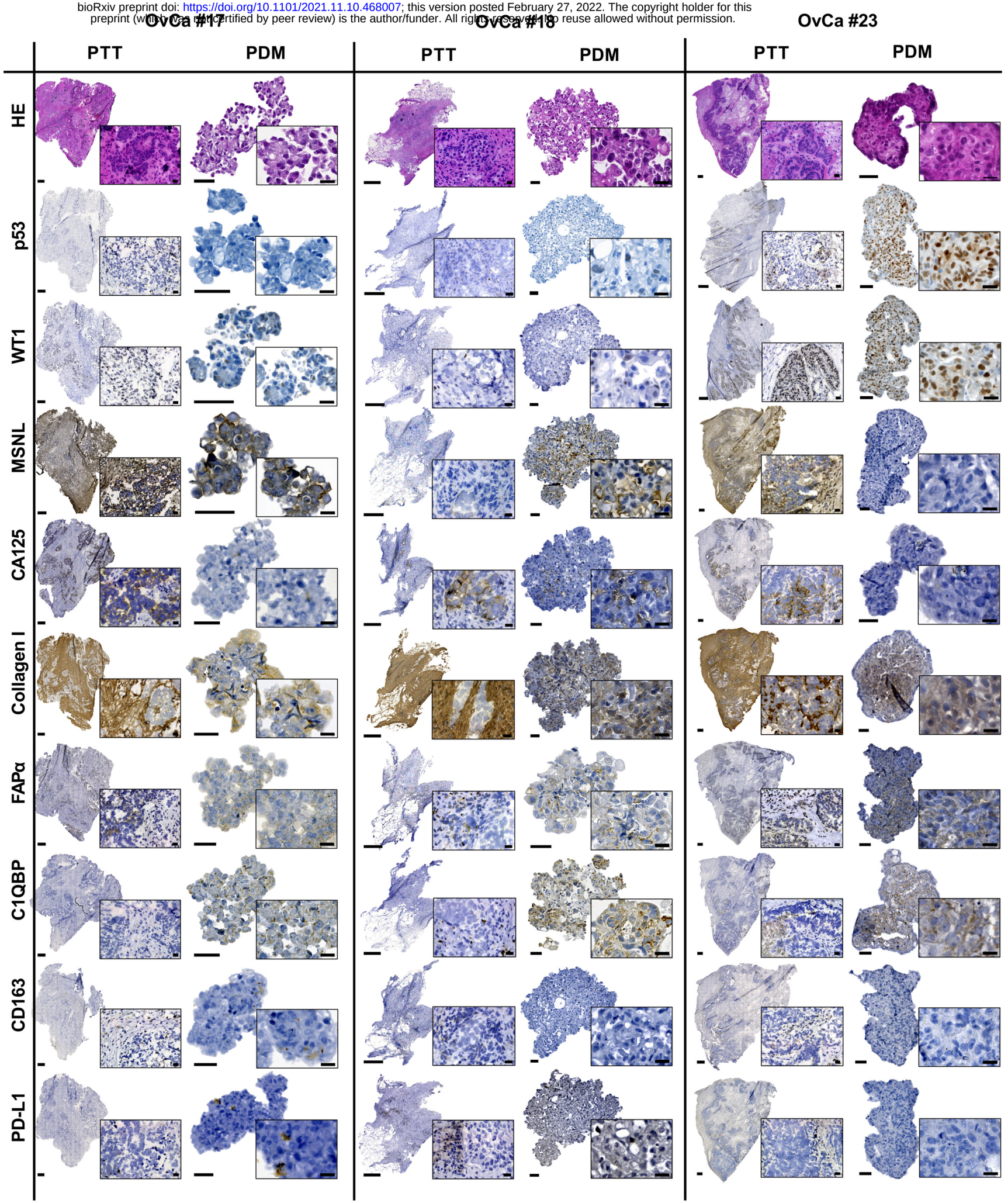

bioRxiv preprint doi: https://doi.org/10.1101/2021.11.10.468007; this version posted February 27, 2022. The copyright holder for this preprint (which was not certified by peer review) is the author/funder. All rights reserved. No reuse allowed without permission.

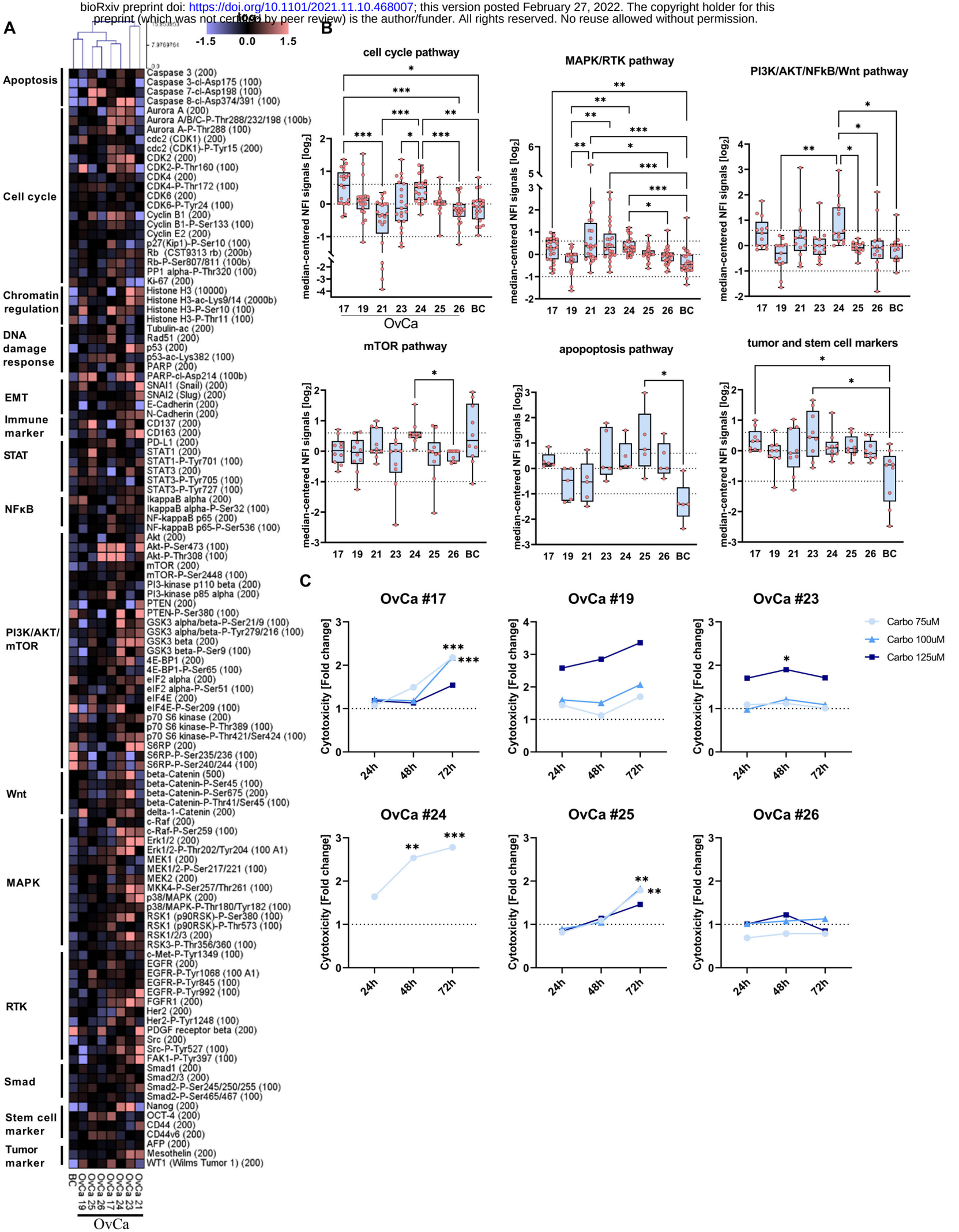

bioRxiv preprint doi: https://doi.org/10.1101/2021.11.10.468007; this version posted February 27, 2022. The copyright holder for this preprint (which was not certified by peer review) is the author/funder. All rights reserved. No reuse allowed without permission.

A

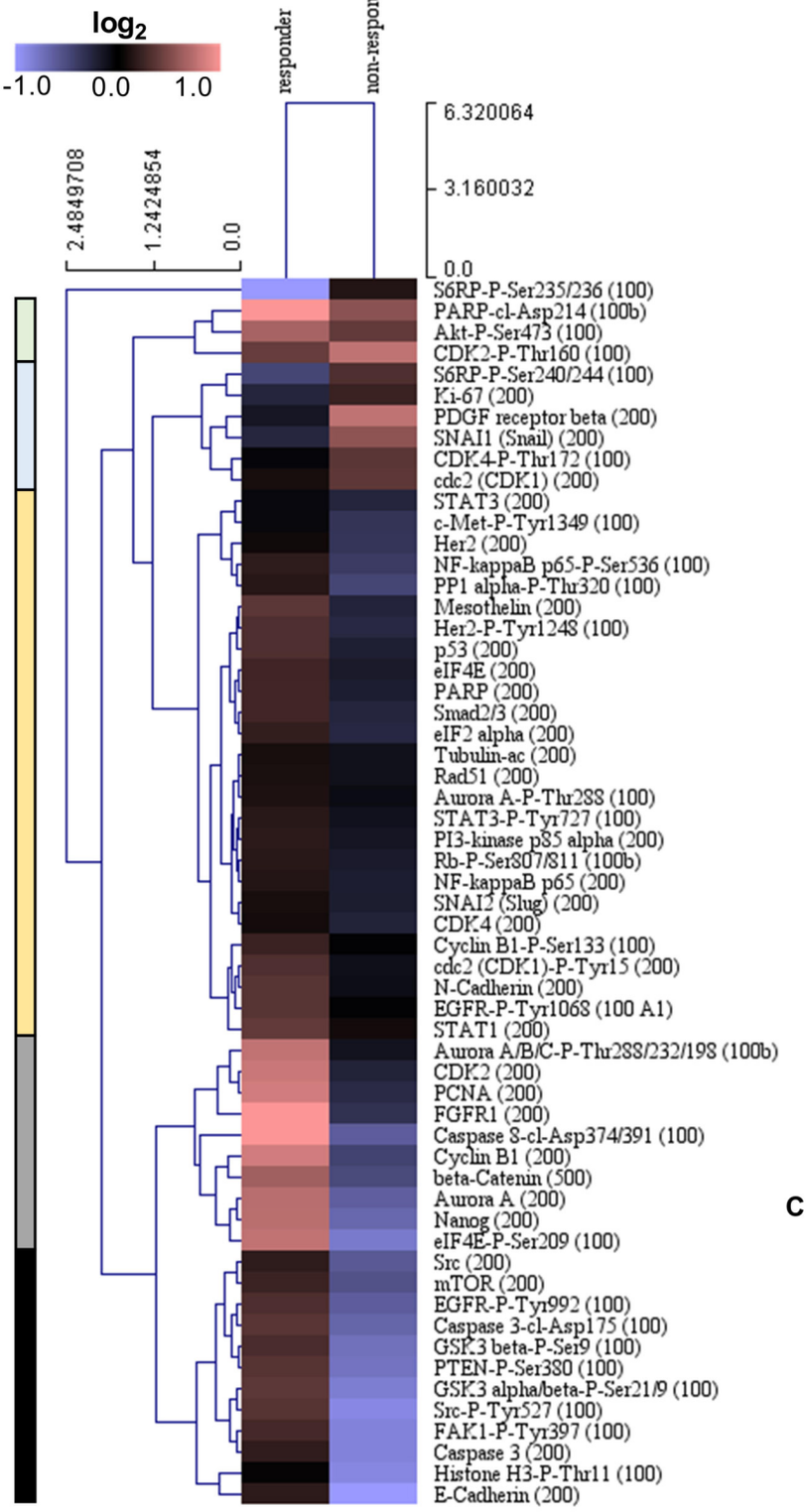

High expression in R and Non-R
High expression in Non-R
Moderate expression in R
High expression in R
Low expression in Non-R

B

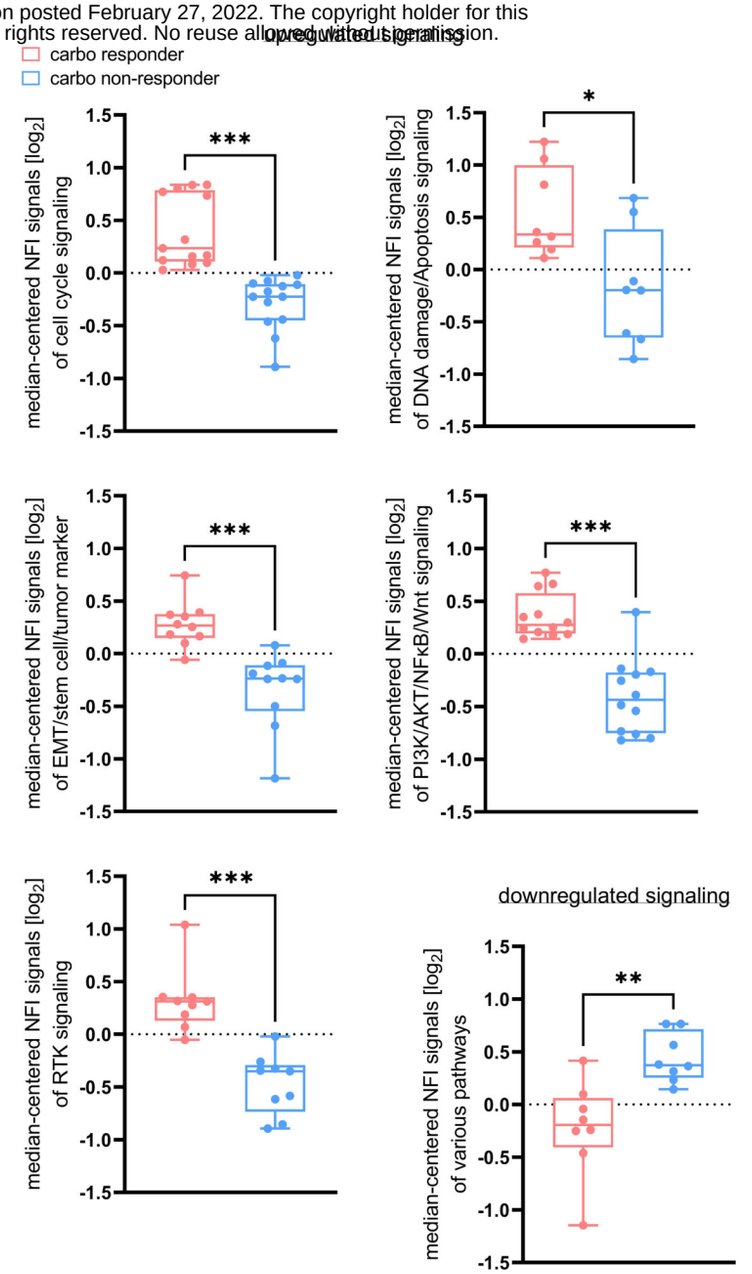

C

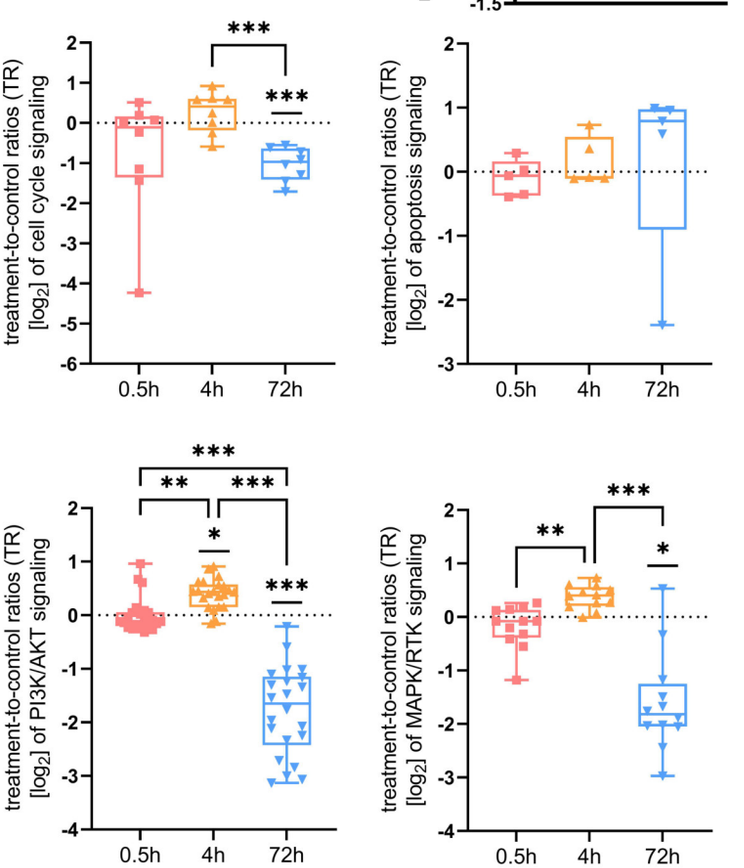
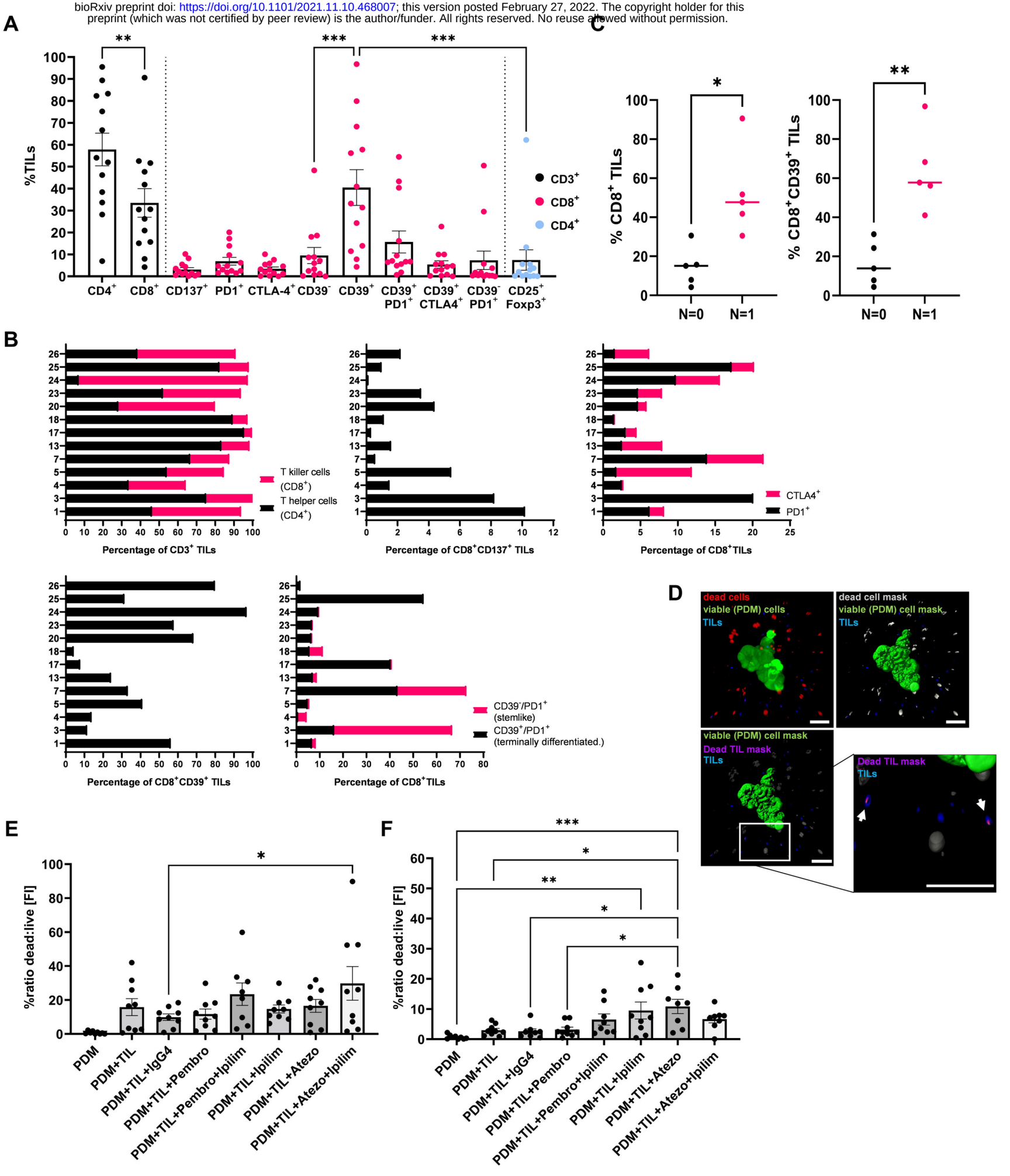
bioRxiv preprint doi: https://doi.org/10.1101/2021.11.10.468007; this version posted February 27, 2022. The copyright holder for this preprint (which was not certified by peer review) is the author/funder. All rights reserved. No reuse allowed without permission.